Ore Geology Reviews 128 (2021) 103924

Contents lists available at ScienceDirect

Ore Geology Reviews

journal homepage: www.elsevier.com/locate/oregeorev

# Mineralogy, geochemistry, and genesis of the Chahgaz (XIVA Anomaly) Kiruna-type iron oxide-apatite (IOA) deposit, Bafq district, Central Iran

Samaneh Ziapour [a], Dariush Esmaeily [a,*], Khalegh Khoshnoodi [b], Shojaodin niroomand [a], Adam C. Simon [c]

[a] Department of Geology, Faculty of Sciences, University of Tehran, Tehran, Islamic Republic of Iran
[b] Nuclear Science and Technology Research Institute, Nuclear Fuel Cycle Research School, Tehran, Islamic Republic of Iran
[c] Department of Earth and Environmental Sciences, University of Michigan, 1100 North University Avenue, Ann Arbor, MI 48109-1005, USA

ARTICLE INFO

*Keywords:*
Chahgaz
Bafq metallogenic province
Magnetite-apatite deposit
Kiruna-type
Hydrothermal alteration
Oxygen isotope
Sulfur isotope

ABSTRACT

The Chahgaz iron oxide-apatite (IOA) deposit is one of the main IOA deposits in the Bafq metallogenic province, Central Iran. The Chahgaz mineral deposit is hosted by Early Cambrian felsic to intermediate, altered subvolcanic to effusive rocks that range compositionally from granite to diorite. Geochemical, geochronologic and tectonomagmatic investigations of various host rock types in the Bafq province indicate that mineralization was the product of Early Cambrian active continental margin processes that evolved calc-alkaline felsic igneous rocks followed by formation of diabase dykes in a back-arc basin environment. Magnetite is present in massive magnetite-rich ore bodies and veinlets that cut the massive ore bodies. Detailed macro- and micro-scopic characterization of mineralized samples and host rocks reveals a paragenetic sequence containing three generations of magnetite that are distinguished from one another compositionally and texturally. The massive ores contain apatite in trace amounts, consistent with IOA deposits globally, and locally exhibit textures that are visually similar to lava flow structures, as described for the El Laco IOA deposit, Chile. The ore bodies contain miarolitic cavities that are filled by calcite, hematite and quartz. The host rocks for the Chahgaz deposit have undergone widespread hydrothermal metasomatism including Na-Ca, K-, Mg-, Si-, sericitic, argillic and carbonatization alteration. The compositions of two generations of magnetite, referred to as Mag1 and Mag2, in massive ore overlap compositions reported for igneous and high-temperature magmatic-hydrothermal magnetite. The third generation of magnetite, which is referred to as Mag3 and is present in veinlets cross-cutting the massive magnetite ore bodies, overlaps compositions reported for low to moderate temperature magmatic-hydrothermal magnetite. Pyrite is present as disseminated grains coeval with Mag1 and micro-fracture filling in the massive magnetite-rich ore bodies.

The $\delta^{18}O$ values obtained for magnetite from representative samples of massive magnetite Mag1 ore range between 2.18 and 6.32‰ and are consistent with $\delta^{18}O$ values reported for igneous and magmatic-hydrothermal magnetite from other deposits in the Bafq district and globally. The $\delta^{34}S$ values for pyrite range from 22.54 to 24.94‰ and are consistent with an evaporitic sulfur source; plausibly by magma contamination with evaporitic rocks of the Early Cambrian Volcano-Sedimentary Sequence (ECVSS). The data presented here are consistent with formation of the massive magnetite-rich ore bodies in the Chahgaz IOA deposit by an iron-rich magmatic-hydrothermal fluid.

## 1. Introduction

Kiruna-type iron oxide-apatite (IOA) deposits occur world-wide and are generally associated with volcanic and intrusive rocks of acidic to basic composition and calc-alkaline affinity (Hitzman, 2000; Groves et al., 2010). A wide variety of hydrothermal alteration/metasomatism is spatially associated with IOA deposits (Hitzman, 2000; Williams et al., 2005; Mumin et al., 2007; Stosch et al., 2011). The genesis of IOA deposits remains controversial with several working hypotheses proposed to explain their formation. The first hypothesis invokes liquid immiscibility where a parent calc-alkaline silicate melt unmixes to yield Fe-P-rich melt and conjugate Si-rich melt, with the Fe-rich melt cooling and

* Corresponding author.
*E-mail address:* esmaili@khayam.ut.ac.ir (D. Esmaeily).

https://doi.org/10.1016/j.oregeorev.2020.103924
Received 11 May 2020; Received in revised form 5 November 2020; Accepted 7 December 2020
Available online 9 December 2020

crystallizing to form a magnetite-rich IOA mineral deposit (Naslund et al., 2002; Tornos et al., 2016, 2017; Velasco et al., 2016; Hou et al., 2018). The second hypothesis invokes formation by hydrothermal fluids of sedimentary origin, e.g., basinal brine or salares, that convect through large volumes of crust where they scavenge iron and phosphorus and precipitate magnetite and apatite during channelized return flow of ore the fluid to shallow crustal levels (Barton and Johnson, 1996; Rhodes et al., 1999; Rhodes and Oreskes, 1999; Sillitoe and Burrows, 2002; Williams et al., 2005; Barton, 2014). A third hypothesis proposes a model that combines igneous and magmatic-hydrothermal processes in which igneous magnetite and exsolved magmatic-hydrothermal fluid form a fluid-magnetite suspension within parent calc-alkaline silicate magma and ascends into the superjacent environment along pre-existing faults to form an IOA deposit (Knipping et al., 2015a, 2015b; Bilenker et al., 2016; Reich et al., 2016; Deditius et al., 2018; Ovalle et al., 2018; Rojas et al., 2018a, 2018b; Simon et al., 2018; Palma et al., 2019, 2020; Childress et al., 2020ab, 2020a, 2020b; Rodriguez-Mustafa et al., 2020). The majority of the research supporting the latter magnetite-fluid suspension hypothesis has been focused on Chilean IOA deposits, and supporting evidence has also been presented in studies of other districts including the namesake Kiruna system in Sweden (Westhues et al., 2016, 2017a, 2017b) and Missouri, USA (Childress et al., 2016).

The Bafq mining district of Central Iran is a well known, world-class mining district that contains more than 2 billion tons of iron ore distributed among dozens of Kiruna-type IOA mineral deposits, with more than 40 identified major magnetic exploration targets (Torab and Lehmann, 2007; Stosch et al., 2011). The economically most important IOA deposits of the Bafq district include Choghart, Se-Chahun, Chadormalu and Chahgaz (Förster and Jafarzadeh, 1994; Daliran, 2002; Moore and Modabberi, 2003). The genesis of mineral deposits in the Bafq district remains debated despite a large and growing body of published research (Förster and Jafarzadeh, 1994; Daliran, 2002; Moore and Modabberi, 2003; Torab and Lehmann, 2007; Jami et al., 2007; Mohseni and Aftabi, 2015; Heidarian et al., 2017). Here we focus on the Chahgaz IOA deposit, also known as Anomaly XIVA, located 43 km north of the Choghart IOA deposit in the Bafq district, Central Iran (Fig. 1a, b).

Although the Chahgaz deposit is one of the largest and most important IOA mines in the Bafq district, it's genesis remains unconstrained. We present and discuss mineral composition data for magnetite and associated alteration assemblages (i.e., amphibole and pyroxene) and conventional stable oxygen for magnetite and sulfur isotope data for pyrite from representative samples of IOA mineralization and host rocks. The new results are compared to published data from other deposits in the Bafq district as well as districts globally and are a major advance in our understanding of the formation of the Chahgaz deposit.

## 2. Geological setting

### 2.1. Regional geology

The tectonically active Iranian Plateau within the Alpine-Himalayan orogenic belt consists of several welded fragments bounded by major faults. The three major structural zones of Central Iran are the Yazd, Tabas and Lut blocks from east to west, which are defined by regional-scale, right-lateral, strike-slip faults (Fig. 1a). The Bafq district is

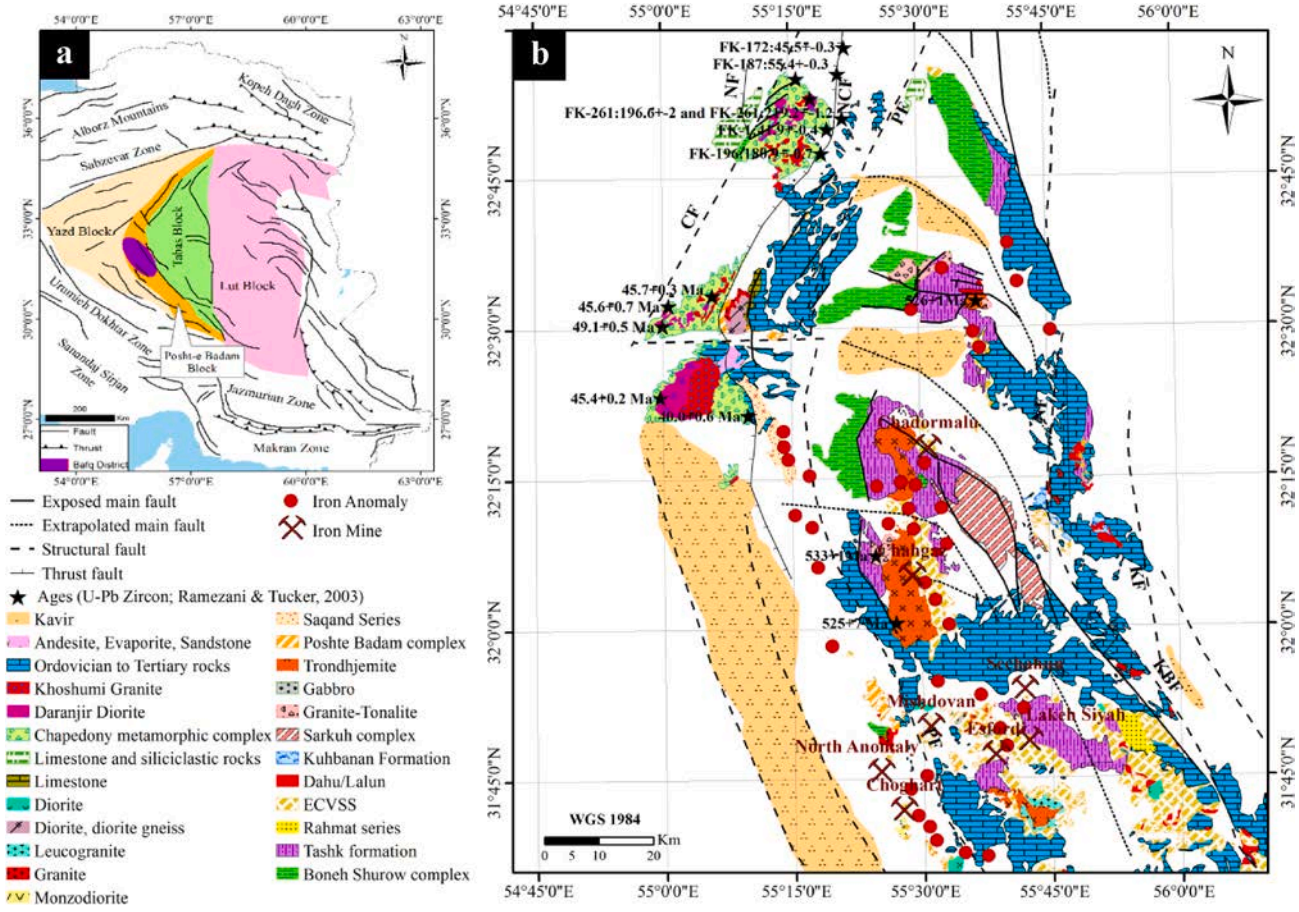


**Fig. 1.** (a) Location of Central Iranian Microplate, major blocks and faults (modified from Haghipour and Aghanabati, 1989); (b) Simplified geological map of the Bafq district showing distribution of iron oxide–apatite deposits (Modified after Ramezani and Tucker, 2003; Rajabi et al., 2015; Khoshnoodi et al., 2017). KBF: Kuhbanan Fault, KF: Kalmard Fault, PF: Posht-e-Badam Fault, CF: Chapedony Fault, NF: Naein Fault.

located in the center of the Posht-e-Badam Block (Stocklin, 1968) or Kashmar-Kerman belt (Ramezani and Tucker, 2003), a part of the Central Iranian microcontinent (Fig. 1a). The Posht-e-Badam Block is situated between the Yazd and Tabas zones that are defined by the Chapedony, Kalmard and Kuhbanan faults and consist of a complex of supracrustal rocks (Alavi, 1991; Aghanabati, 2008).

The Bafq district hosts a thick sequence including Neoproterozoic crystalline basement, Paleozoic (Early Cambrian to Tertiary) rocks and younger units (Förster and Jafarzadeh, 1994). The Precambrian basement in the Bafq district is characterized by Late Neoproterozoic medium- to high- grade metamorphic rocks of the Boneh-Shurow and Posht-e-Badam complexes that are intruded by granitic intrusions of Triassic age (Fig. 1b; Ramezani and Tucker, 2003; Jami et al., 2007; Rajabi, 2012). The Posht-e-Badam complex, exposed in west of the Posht-e-Badam Fault, is a composite of greenstone, schist, marble, amphibolite, pyroxenite, serpentinite, gneiss, *meta*-basalts and conglomerate (Haghipour and Pelissier, 1977). The Boneh-Shurow complex consists of a 2000-m-thick metamorphic unit exposed in east of the Posht-e-Badam Fault, including gneiss, green micaschist and amphibolite (Fig. 1b; Haghipour and Pelissier, 1977; Aghanabati, 2008). The U-Pb Zircon dating of this complex by Ramezani and Tucker (2003) showed an age of 602–617 Ma.

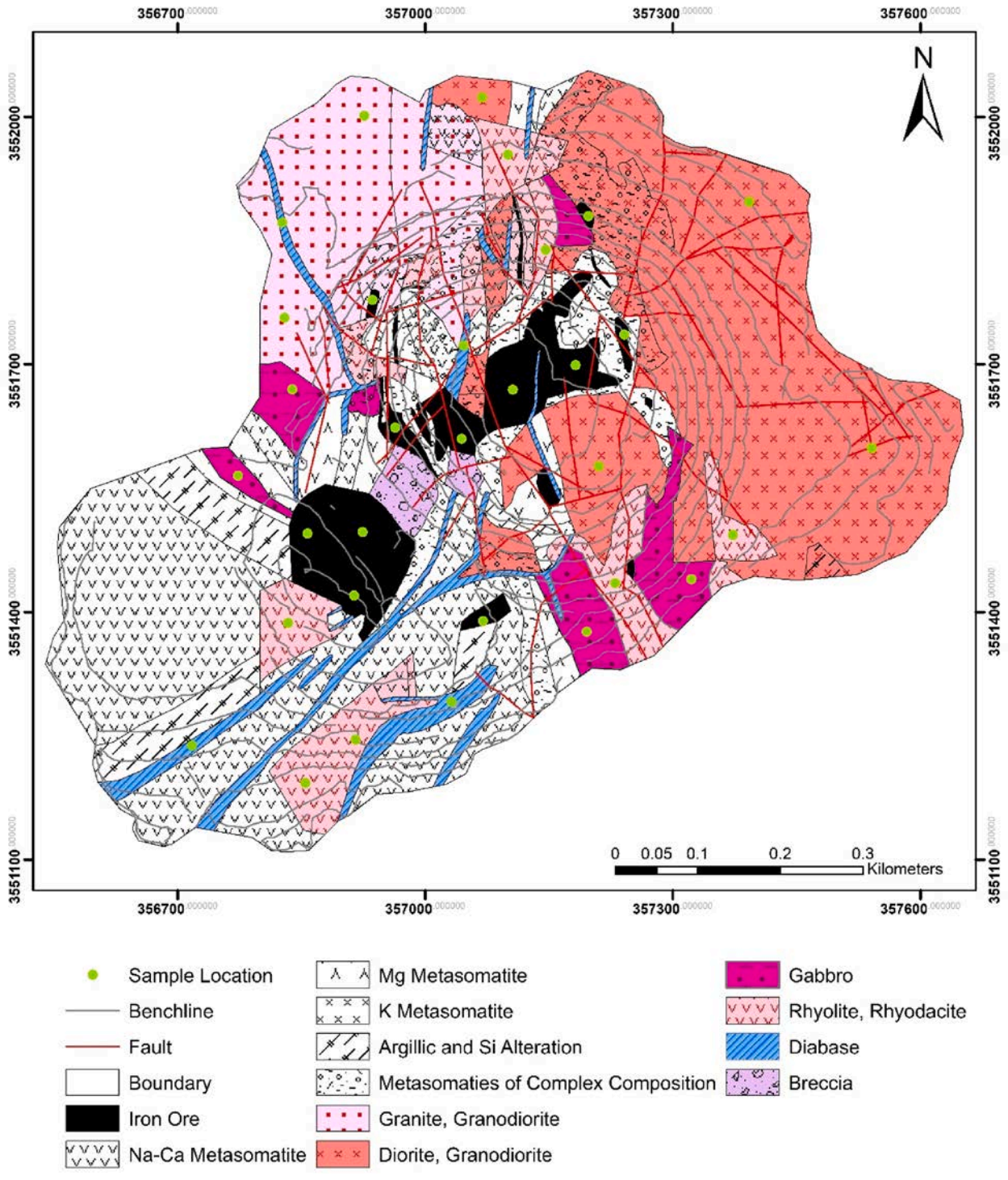


**Fig. 2.** Geological map of the Chahgaz iron deposit (modified after Kavoshgaran Consultant Engineers, 2009).

A 2000 m thick sequence of Late Proterozoic-Early Cambrian phyllite, slate, quartzite, marble, quartzitic schist, gneiss, basalt, tuffaceous rocks, limestone, argillite and sandstone belonging to the Tashk Formation covers the Boneh-Shurow complex (Ramezani and Tucker, 2003). The Tashk Formation is covered by 2500-m-thick bimodal volcanic unit and volcano-sedimentary rocks of the Early Cambrian volcano-sedimentary sequence (ECVSS, 530–528 Ma). The ECVSS has been introduced as the Cambrian Volcano-Sedimentary Unit (CVSU) (Ramezani and Tucker, 2003), Rizu and Desu series (Huckriede et al., 1962), as well as Esfordi Formation (Borumandi, 1973). The ECVSS is dominated by basal conglomerate, basaltic and rhyolitic lavas, tuffaceous shale, sandstone and evaporitic intercalations, shale, pyroclastic and epiclastic rocks, limestone and gypsiferous dolomite, intruded by late diabase dikes (Rajabi, 2012; Ramezani and Tucker, 2003; Jami, 2005). The ECVSS in the Bafq metallogenic district hosts the important world-class Kiruna-type IOA, Fe-Mn exhalative and Zn-Pb SEDEX-type deposits as well as REE-U-T mineralization (Daliran, 2002, Jami et al., 2007; Torab and Lehmann, 2007; Stosch et al., 2011). Iron oxide-apatite deposits in the Bafq district formed during the Early Cambrian, associated with felsic volcanics and regional- to deposit-scale metasomatic alteration (Stosch et al., 2011).

### 2.2. Mine-scale geology

The Chahgaz deposit in the eastern contact of Zarigan granitoid is composed of two separate massive ore bodies in the form of vertical pipe shaped bodies that are approximately 690 m deep, and are referred to as the eastern and western ore bodies. The deposit resource is 83.1 Mt at 53.16% Fe and 0.49% P. The mineralization zone is controlled by mine-scale NE-SW and NW-SE faults (Fig. 2). Observations in the field indicate that mineralization originally consisted of one ore body that was subsequently dissected into two ore bodies by a NW-SE strike-slip fault. As a result, there is a tectono-hydrothermal brecciated zone between the ore bodies. The ore bodies dominantly display sharp contacts with altered rocks.

The Chahgaz ore deposit is mainly hosted in the ECVSS, which is dominated by felsic lava flows and shallow felsic-intermediate subvolcanic rocks (Förster and Jafarzadeh, 1994). The host rocks have undergone extensive hydrothermal alteration where the extent of alteration often follows fault orientation (Förster and Jafarzadeh, 1994; Kavoshgaran Consultant Engineers, 2009). The original features of the host rocks can be recognized with increasing distance from the ore bodies. The U-Pb zircon dating by Ramezani and Tucker (2003) yield 533 ± 1 Ma for the emplacement of Zarigan granitoid and 528 ± 1 Ma for dacite-porphyry and rhyodacite near Chahgaz deposit. Younger

**Table 1**
Whole rock compositions of plutonic and volcanic host rocks and diabase dikes in the Chahgaz mineral deposit.

| Sample No. | Rock Type | $Al_2O_3$ | CaO | $Fe_2O_3$ | $K_2O$ | MnO | MgO | $Na_2O$ | $P_2O_5$ | $SiO_2$ | $TiO_2$ |
|---|---|---|---|---|---|---|---|---|---|---|---|
| | | % | % | % | % | % | % | % | % | % | % |
| ChG-17 | Diorite | 13.58 | 5.36 | 11.52 | 1.19 | 0.18 | 4.10 | 4.54 | 0.27 | 55.45 | 1.72 |
| ChG-18 | Rhyodacite | 11.91 | 1.44 | 5.59 | 1.53 | 0.07 | 0.90 | 4.87 | 0.17 | 67.46 | 0.86 |
| ChG-19 | Rhyodacite | 12.78 | 1.96 | 7.65 | 1.54 | 0.12 | 1.10 | 5.33 | 0.19 | 67.56 | 0.93 |
| ChG-26 | Rhyolite | 11.68 | 3.27 | 0.30 | 7.81 | 0.01 | 0.09 | 0.17 | 0.02 | 69.72 | 0.10 |
| ChG-32 | Rhyolite | 11.05 | 0.36 | 2.55 | 6.44 | 0.02 | 2.06 | 1.77 | 0.02 | 72.35 | 0.09 |
| ChG-45 | Quartz-diorite | 13.18 | 2.84 | 8.74 | 0.30 | 0.14 | 1.43 | 6.99 | 0.38 | 62.56 | 1.31 |
| ChG-49 | Diorite | 11.75 | 4.71 | 11.42 | 1.39 | 0.18 | 3.86 | 4.48 | 0.26 | 56.35 | 1.05 |
| ChG-53 | Diorite | 12.68 | 4.76 | 10.90 | 0.93 | 0.19 | 2.22 | 5.35 | 0.47 | 57.40 | 1.82 |
| ChG-78 | Diabase | 15.87 | 4.66 | 12.07 | 0.78 | 0.06 | 8.51 | 4.69 | 0.13 | 48.48 | 1.34 |
| ChG-79 | Gabbro | 14.44 | 6.14 | 15.16 | 1.18 | 0.14 | 4.66 | 4.27 | 0.37 | 44.84 | 3.64 |
| ChG-80 | Gabbro | 15.16 | 6.30 | 15.08 | 1.52 | 0.20 | 4.89 | 3.81 | 0.37 | 45.61 | 3.25 |
| ChG-81 | Gabbro | 14.38 | 5.64 | 15.24 | 1.78 | 0.15 | 5.04 | 3.42 | 0.36 | 45.29 | 3.25 |
| ChG-82 | Gabbro | 12.59 | 7.79 | 15.16 | 1.10 | 0.12 | 4.29 | 3.84 | 0.32 | 46.45 | 3.55 |
| ChG-83 | Rhyodacite | 14.99 | 11.89 | 1.52 | 1.63 | 0.20 | 0.58 | 5.48 | 0.22 | 46.90 | 0.75 |
| ChG-110 | Rhyolite | 9.10 | 0.20 | 1.59 | 6.47 | 0.00 | 0.18 | 0.13 | 0.02 | 83.20 | 0.10 |
| ChG-112 | Rhyolite | 11.01 | 0.27 | 0.77 | 7.75 | 0.00 | 0.19 | 0.17 | 0.03 | 72.70 | 0.13 |
| ChG-144 | Granite | 8.88 | 2.36 | 1.34 | 2.64 | 0.04 | 1.98 | 5.29 | 0.00 | 66.55 | 0.09 |
| ChG-161 | Diabase | 11.53 | 3.37 | 16.09 | 0.24 | 0.04 | 4.61 | 5.19 | 1.05 | 49.76 | 3.54 |
| ChG-166 | Diabase | 13.47 | 2.92 | 11.52 | 3.73 | 0.03 | 6.81 | 3.76 | 0.23 | 48.84 | 2.70 |
| ChG-168 | Diabase | 13.14 | 1.13 | 19.00 | 0.12 | 0.02 | 7.28 | 5.30 | 0.18 | 46.81 | 1.90 |
| ChG-186 | Granite | 11.67 | 2.84 | 8.39 | 1.67 | 0.11 | 0.96 | 5.08 | 0.21 | 62.98 | 0.96 |
| Sample No. | Type of Sample (Core/Outcrop) | $V_2O_5$ | Total | Ce | Co | Hf | Nb | Ta | Th | Y | Zr |
| | | % | % | ppm | ppm | ppm | ppm | ppm | ppm | ppm | ppm |
| ChG-17 | Outcrop | 0.03 | 97.94 | 67 | 25.6 | 2.08 | 15.9 | 1.13 | 3.95 | 82.1 | 48 |
| ChG-18 | Outcrop | 0.01 | 94.81 | 121 | 5.9 | 4.73 | 19 | 1.29 | 6.73 | 91.9 | 284 |
| ChG-19 | Outcrop | 0.01 | 99.17 | 137 | 9.1 | 5.21 | 21.4 | 1.37 | 5.79 | 115.3 | 320 |
| ChG-26 | Outcrop | 0.01 | 93.18 | 320 | 1.4 | 2.41 | 4.3 | 0.53 | 213.16 | 54.2 | 164 |
| ChG-32 | Outcrop | 0.01 | 96.72 | 18 | 5.7 | 2.75 | 2.5 | 0.48 | 5.52 | 12.9 | 153 |
| ChG-45 | Outcrop | 0.01 | 97.88 | 92 | 9.7 | 3.27 | 20.3 | 1.32 | 4.73 | 91.8 | 75 |
| ChG-49 | Outcrop | 0.02 | 95.47 | 72 | 24.7 | 3.5 | 16.2 | 1.19 | 4.61 | 82.4 | 66 |
| ChG-53 | Outcrop | 0.02 | 96.74 | 90 | 15.8 | 2.03 | 18.5 | 1.25 | 4.17 | 102.1 | 47 |
| ChG-78 | Outcrop | 0.03 | 96.62 | 33 | 34.5 | 2.31 | 7.2 | 0.83 | 9.07 | 32.2 | 80 |
| ChG-79 | Core | 0.02 | 94.86 | 68 | 48.3 | 4.87 | 39.9 | 2.33 | 2.41 | 21.1 | 157 |
| ChG-80 | Core | 0.02 | 96.21 | 57 | 50.3 | 3.89 | 35.8 | 2.15 | 1.85 | 17.8 | 117 |
| ChG-81 | Core | 0.02 | 94.57 | 50 | 53.4 | 3.52 | 34.8 | 2.04 | 3.46 | 16.8 | 99 |
| ChG-82 | Core | 0.02 | 95.23 | 66 | 40.1 | 5.43 | 35.6 | 2.01 | 2.73 | 21.2 | 162 |
| ChG-83 | Core | 0.01 | 84.17 | 83 | 3.6 | 4.69 | 16.9 | 1.14 | 4.99 | 29.2 | 234 |
| ChG-110 | Outcrop | 0.01 | 101 | 7 | 0.75 | 3.22 | 3.2 | 0.42 | 14.3 | 6.5 | 185 |
| ChG-112 | Outcrop | 0.01 | 93.03 | 13 | 0.75 | 4.05 | 4.5 | 0.54 | 13.56 | 12 | 385 |
| ChG-144 | Outcrop | 0.01 | 89.18 | 14 | 1.9 | 4.07 | 4.2 | 0.57 | 19.46 | 20.9 | 96 |
| ChG-161 | Outcrop | 0.03 | 95.45 | 54 | 21 | 2.95 | 6.1 | 0.6 | 1.65 | 62.2 | 82 |
| ChG-166 | Core | 0.04 | 94.05 | 23 | 31.1 | 2.11 | 5 | 0.53 | 0.7 | 30.4 | 25 |
| ChG-168 | Core | 0.04 | 94.92 | 50 | 22.5 | 1.39 | 4.8 | 0.45 | 2.13 | 27.7 | 41 |
| ChG-186 | Core | 0.01 | 94.88 | 189 | 10 | 4.11 | 23.8 | 1.49 | 6.6 | 126 | 82 |

diabasic dikes were emplaced into all host rock types and the ore bodies, which suggests the presence of mafic intrusions in depth (Förster and Jafarzadeh, 1994; Kavoshgaran Consultant Engineers, 2009).

## 3. Methodology

The current study is based on field observations and sampling of outcrop and drill core at the Chahgaz deposit. The locations of collected samples are shown on Fig. 2. Representative mineralized samples and host rocks, as well as diabase dikes, were collected for petrography, mineralogy, field emission scanning electron microscopy (FE-SEM), electron probe microanalysis (EPMA), and stable O and S isotopic compositions. Whole-rock major and trace element compositions for representative samples of least-altered host rocks and diabase dikes (4 samples from diabase dikes, 7 samples from volcanic host rocks and 10 samples from plutonic host rocks) were used for geochemical classification and tectonic setting. The whole-rock concentrations were determined by Inductively Coupled Plasma Optical Emission Spectrometry (ICP-OES) and Mass Spectrometry (ICP-MS) at Zarazma laboratory in Tehran, Iran (Table 1). Detection limits are <10 ppm for major elements and <0.01 ppm for trace elements. All samples were studied petrographically by using an Olympus BX60 microscope at the petrography laboratory at the University of Tehran. Detailed studies of mineral assemblages, alteration and metasomatic replacements were performed on selected samples by using FE-SEM and EPMA (Table 2). The FESEM study was performed at the Center for Applied Research of the Geological Survey and Mineral Exploration of Iran, Karaj, using a SIGMA/VP-ZEISS FE-SEM equipped with an X-Max Oxford electron

**Table 2**
Representative electron probe microanalyses (EPMA) of magnetite from magnetite, amphibole and pyroxene from altered host rocks in the Chahgaz mineral deposit (in wt. %; L: lighter magnetite, D: darker magnetite; BDL: below detection limit).

| No. | $Na_2O$ | $K_2O$ | MgO | CaO | MnO | FeO | CoO | NiO | CuO | ZnO | $Al_2O_3$ | $V_2O_3$ | $Cr_2O_3$ | $SiO_2$ | $TiO_2$ | Total |
|---|---|---|---|---|---|---|---|---|---|---|---|---|---|---|---|---|
| | Magnetite 1 | | | | | | | | | | | | | | | |
| O-1(L) | BDL | BDL | 0.05 | BDL | 0.04 | 92.2 | 0.44 | 0.36 | 0.09 | 0.07 | 0.03 | 0.52 | 0.03 | 0.04 | 0.03 | 93.86 |
| O-2(L) | BDL | BDL | BDL | BDL | 0.03 | 91.33 | 0.03 | BDL | 0.06 | 0.18 | 0.03 | 0.49 | 0.03 | 0.08 | 0.11 | 92.34 |
| O-3(L) | BDL | BDL | BDL | 0.07 | 0.05 | 91.89 | 0.03 | BDL | 0.23 | 0.18 | 0.03 | 0.53 | 0.04 | 0.04 | 0.03 | 93.03 |
| O-4(L) | BDL | BDL | 0.03 | BDL | 0.03 | 92.33 | 0.03 | BDL | 0.26 | BDL | 0.06 | 0.46 | 0.05 | 0.12 | 0.03 | 93.34 |
| O-5(L) | BDL | BDL | BDL | 0.03 | 0.03 | 92.07 | 0.33 | BDL | 0.16 | 0.12 | 0.03 | 0.48 | 0.04 | 0.03 | 0.03 | 93.28 |
| O-6(D) | 0.13 | BDL | 0.02 | BDL | 0.04 | 91.73 | 0.03 | 0.14 | 0.1 | BDL | 0.03 | 0.51 | 0.03 | 0.08 | 0.49 | 93.27 |
| O-7(D) | BDL | BDL | BDL | BDL | 0.03 | 90.88 | 0.03 | 0.36 | 0.34 | 0.15 | 0.03 | 0.52 | 0.06 | 0.03 | 0.74 | 93.11 |
| O-8(L) | BDL | BDL | BDL | BDL | 0.03 | 91.36 | 0.6 | 0.16 | 0.03 | 0.33 | 0.04 | 0.51 | 0.03 | 0.16 | 0.05 | 93.24 |
| O-9(L) | BDL | BDL | BDL | BDL | 0.05 | 91.61 | 0.28 | 0.06 | 0.03 | BDL | 0.03 | 0.49 | 0.05 | 0.04 | 0.03 | 92.6 |
| O-10(D) | BDL | BDL | 0.01 | 0.03 | 0.03 | 79.78 | 0.69 | 0.18 | 0.03 | BDL | 0.03 | 1.14 | 0.07 | 0.03 | 6.59 | 88.55 |
| O-11(D) | 0.18 | BDL | 0.01 | 0.03 | 0.03 | 82.93 | 0.16 | BDL | 0.24 | 0.05 | 0.04 | 1.19 | 0.13 | 0.08 | 5.89 | 90.93 |
| O-12(D) | 0.13 | BDL | 0.2 | 0.06 | 0.03 | 87.61 | 0.84 | BDL | 0.03 | BDL | 0.08 | 0.64 | 0.13 | 0.22 | 1.5 | 91.41 |
| O-13(D) | 0.11 | BDL | 0.03 | 0.1 | 0.03 | 85.56 | 0.21 | 0.16 | 0.11 | BDL | 0.05 | 0.87 | 0.07 | 0.08 | 3.3 | 90.65 |
| O-14(D) | BDL | BDL | 0.01 | 0.04 | 0.03 | 83.67 | 0.03 | 0.1 | 0.03 | BDL | 0.03 | 1.17 | 0.1 | 0.06 | 6 | 91.17 |
| O-15(L) | BDL | BDL | BDL | BDL | 0.03 | 89.52 | 0.03 | 0.67 | 0.03 | BDL | 0.03 | 0.48 | 0.12 | 0.12 | 0.03 | 90.99 |
| O-16(L) | BDL | BDL | 0.01 | 0.01 | 0.06 | 88.02 | 0.32 | 0.22 | 0.08 | 0.04 | 0.03 | 0.48 | 0.1 | 0.05 | 0.03 | 89.39 |
| O-17(L) | BDL | BDL | BDL | 0.01 | 0.03 | 89.12 | 0.03 | BDL | 0.03 | BDL | 0.03 | 0.5 | 0.13 | 0.07 | 0.03 | 89.83 |
| O-18(L) | BDL | BDL | BDL | 0.04 | 0.03 | 89.8 | 0.03 | 0.49 | 0.03 | 0.13 | 0.03 | 0.47 | 0.03 | 0.04 | 0.73 | 91.72 |
| O-19(D) | BDL | BDL | BDL | 0.15 | 0.03 | 89.56 | 0.03 | BDL | 0.03 | 0.05 | 0.03 | 0.52 | 0.04 | 0.05 | 1.03 | 91.4 |
| | Magnetite 2 | | | | | | | | | | | | | | | |
| O-20(L) | BDL | BDL | 0.03 | 0.08 | 0.03 | 89.36 | 0.03 | BDL | 0.03 | BDL | 0.04 | 0.49 | 0.06 | 0.11 | 0.03 | 90.18 |
| O-21(L) | BDL | BDL | 0.12 | 0.19 | 0.03 | 90.55 | 0.03 | 0.08 | 0.17 | BDL | 0.04 | 0.43 | 0.07 | 0.21 | 0.02 | 91.88 |
| O-22(L) | BDL | BDL | 0.01 | 0.21 | 0.03 | 90.14 | 0.03 | BDL | 0.03 | 0.05 | 0.03 | 0.36 | 0.03 | 0.09 | 0.11 | 91.03 |
| O-23(L) | BDL | BDL | 0.01 | 0.48 | 0.03 | 89.65 | 0.03 | 0.11 | 0.03 | BDL | 0.03 | 0.39 | 0.11 | 0.05 | 0.01 | 90.82 |
| O-24(L) | BDL | BDL | 0.03 | 0.49 | 0.03 | 91.59 | 0.03 | 0.64 | 0.08 | 0.11 | 0.03 | 0.38 | 0.03 | 0.12 | 0.19 | 93.71 |
| O-25(D) | BDL | BDL | 0.01 | 0.7 | 0.03 | 83.34 | 0.27 | 0.98 | 0.03 | 0.01 | 0.03 | 1.05 | 0.11 | 0.04 | 4.62 | 91.14 |
| O-26(D) | BDL | BDL | 0.03 | 0.27 | 0.03 | 87 | 0.03 | BDL | 0.03 | 0.06 | 0.12 | 0.6 | 0.08 | 0.09 | 1.35 | 89.61 |
| | Magnetite 3 | | | | | | | | | | | | | | | |
| O-27 | 0 | 0 | 0.03 | 0 | 0.03 | 89.61 | 0.18 | 0.38 | 0.077 | 0 | 0.032 | 0.2 | 0.032 | 0.09 | 0.052 | 90.27 |
| | Clinopyroxene | | | | | | | | | | | | | | | |
| CPX-1 | 2.14 | 0.45 | 21.25 | 12.14 | 0.05 | 6.28 | BDL | 0.02 | BDL | BDL | 1.15 | 0.04 | BDL | 53.62 | 0.25 | 97.39 |
| CPX-2 | 2.49 | 0.49 | 21.8 | 11.96 | BDL | 5.81 | BDL | BDL | BDL | BDL | 1.27 | 0.02 | BDL | 53.28 | 0.3 | 97.44 |
| CPX-3 | 2.88 | 0.57 | 22.28 | 11.53 | 0.06 | 5.79 | BDL | 0.27 | BDL | BDL | 1.7 | 0.06 | BDL | 51.43 | 0.52 | 97.1 |
| CPX-4 | 0.41 | 0.44 | 15.9 | 12.24 | 0.1 | 14.33 | BDL | BDL | BDL | BDL | 3.19 | 0.03 | BDL | 51.03 | 0.07 | 97.78 |
| CPX-5 | 0.33 | 0.08 | 15.44 | 12.87 | 0.04 | 14.69 | BDL | BDL | BDL | BDL | 2.28 | 0.05 | 0.02 | 51.42 | 0.06 | 97.28 |
| CPX-6 | 0.11 | 0.01 | 17.48 | 13.33 | 0.11 | 11.39 | BDL | 0.18 | BDL | BDL | 1.11 | 0.02 | BDL | 54.07 | 0.04 | 97.91 |
| CPX-7 | 0.37 | 0.09 | 17.32 | 13.01 | 0.28 | 10.65 | BDL | BDL | BDL | BDL | 1.5 | 0.02 | BDL | 54.07 | 0.03 | 97.38 |
| CPX-8 | 0.52 | 0.04 | 16.65 | 12.41 | 0.25 | 12.68 | BDL | 0.14 | BDL | BDL | 0.91 | 0.02 | BDL | 54.17 | 0.01 | 97.8 |
| CPX-9 | 0.51 | 0.16 | 17.92 | 13.74 | 0.02 | 10.29 | BDL | BDL | BDL | BDL | 2.71 | 0.02 | 0.02 | 52.36 | 0.15 | 97.9 |
| CPX-10 | 0.28 | 0.08 | 12.72 | 13.66 | 0.13 | 17.45 | BDL | BDL | BDL | BDL | 1.04 | 0.04 | 0.03 | 52.46 | 0.02 | 97.91 |
| CPX-11 | 0.34 | 0.1 | 10.85 | 12.3 | 0.04 | 19.56 | BDL | BDL | BDL | BDL | 1.38 | 0.04 | BDL | 52.48 | 0.01 | 97.1 |
| CPX-12 | 0.4 | 0.17 | 18.15 | 12.79 | 0.08 | 11.34 | BDL | BDL | BDL | BDL | 1.98 | 0.06 | BDL | 52.43 | 0.15 | 97.59 |
| CPX-13 | 0.9 | 0.25 | 18.7 | 13.9 | 0.01 | 9.08 | BDL | BDL | BDL | BDL | 2.28 | 0.03 | BDL | 52.15 | 0.19 | 97.49 |
| | Amphibole | | | | | | | | | | | | | | | |
| AM-1 | 0.22 | 0.04 | 14.52 | 13.08 | 0.04 | 15.45 | BDL | 0.17 | BDL | BDL | 1.07 | 0.02 | 0.02 | 52.45 | BDL | 97.08 |
| AM-2 | 0.19 | 0.03 | 15.44 | 14.9 | 0.02 | 13.19 | BDL | BDL | BDL | BDL | 0.79 | 0.02 | 0.02 | 52.61 | BDL | 97.21 |
| AM-3 | 1.42 | 0.31 | 19.08 | 12.33 | 0.13 | 9.8 | BDL | BDL | BDL | BDL | 1.33 | 0.04 | BDL | 53.39 | 0.25 | 98.16 |
| AM-4 | 0.21 | 0.13 | 15.88 | 13.22 | 0.07 | 12.16 | BDL | 0.04 | BDL | BDL | 1.86 | 0.01 | BDL | 53.66 | 0.07 | 97.33 |
| AM-5 | 0.3 | 0.07 | 13.81 | 13.57 | 0.08 | 14.73 | BDL | BDL | BDL | BDL | 1.45 | 0.02 | BDL | 53.69 | 0.03 | 97.78 |
| AM-6 | 0.12 | 0.07 | 12.99 | 12.95 | 0.06 | 16.72 | BDL | BDL | BDL | BDL | 1.1 | BDL | BDL | 53.15 | BDL | 97.19 |
| AM-7 | 1.65 | 0.32 | 20.77 | 11.51 | 0.04 | 6.36 | BDL | 0.1 | BDL | BDL | 1.59 | 0.03 | BDL | 55.22 | 0.26 | 97.85 |
| AM-8 | 0.68 | 0.17 | 20.11 | 12.76 | 0.05 | 7.6 | BDL | BDL | BDL | BDL | 1.91 | 0.05 | BDL | 54.58 | 0.1 | 98.01 |
| AM-9 | 0.23 | 0.09 | 15.75 | 13.15 | 0.08 | 12.6 | BDL | BDL | BDL | BDL | 2.66 | 0.05 | BDL | 52.76 | 0.03 | 97.43 |
| AM-10 | 0.36 | 0.13 | 18.62 | 12.64 | 0.04 | 10.01 | BDL | BDL | BDL | BDL | 1.52 | 0.05 | BDL | 53.79 | 0.16 | 97.37 |

dispersive spectrometer (EDS). Quantitative determination of mineral compositions was carried out using a Cameca SX-100 EPMA at the mineralogy division of the Iranian Mineral Processing Research Centre, equipped with 5 wavelength-dispersive crystal spectrometers. The EPMA analyses were performed at 15 kV and 20 nA using a defocused 5 μm diameter beam and 15 s counting time for major elements, and at 25 kV and 20nA using a defocused 3 μm diameter beam and 30 s counting time for trace elements. A TiKα-VKβ interference correction was used.

The abundances of $^{16}O$ and $^{18}O$ in magnetite samples were determined at the University of Western Ontario, Canada. For oxygen isotope measurements, magnetite grains without visible impurities were separated under a binocular microscope after crushing and washing in distilled water to avoid grains with impurities. Approximately 8 mg of magnetite were weighed into spring-loaded sample holders, evacuated overnight while heating to 150 °C, and then placed into nickel reaction vessels and heated under active vacuum at 300 °C for 3 h to remove any remaining absorbed water. Samples were then reacted overnight at ca. 580 °C with $ClF_3$ to release silicate- or oxide-bound oxygen. The released oxygen was converted to $CO_2$ over red-hot graphite, followed by isotopic measurement using a Micromass Optima, stable-isotope-ratio mass-spectrometer dual-inlet mode to quantify the abundances of $^{16}O$ and $^{18}O$. The following standards were analyzed during the analyses of Chahgaz samples: in-house quartz, in-house kaolinite, and $CO_2$. The results for the standards were 11.85‰, 21.22‰ and 10.34‰, respectively, and the accepted values are 11.5‰, 21.5‰ and 3.8‰. Standards were measured before, during, and after analysis of Chahgaz magnetite samples to correct for instrumental drift. Individual sample analyses typically have 2σ of <0.1‰. The oxygen isotope data are reported in the standard $\delta^{18}O$ notation in parts per thousand (‰) relative to the international Vienna Standard Mean Ocean Water-Standard Light Antarctic Precipitation (VSMOW-SLAP) reference material 8535A and were calculated by using the following equation.

$$\delta^{18}O_{sample}(‰) = \left[\left(\ ^{18}O/\ ^{16}O\right)_{measured} / \left(\ ^{18}O/\ ^{18}O\right)_{VSMOW} - - 1\right] * 1000$$

VSMOW-SLAP refers to the Vienna SMOW-SLAP δ-scales, which are defined by assigning $\delta^2H$ and $\delta^{18}O$ values of 0‰ to VSMOW2 (RM 8535a) and values of −427.5‰ ($\delta^2H$) and −55.50‰ ($\delta^{18}O$) to measurements of SLAP2 (RM 8537a) for the purpose of normalizing stable hydrogen and oxygen isotope measurements (NIST, 2020).

The abundances of $^{32}S$ and $^{34}S$ in pyrite samples were determined at the Ján Veizer Stable Isotope Laboratory (formerly G.G. Hatch), at the University of Ottawa, Canada following the same procedures described in Grassineau et al. (2001). Pyrite grains were collected by crushing and grinding pyrite-bearing ore samples followed by removing magnetite with a hand magnet and hand-picking pyrite grains using a binocular microscope. Samples without visible impurities were weighed into tin capsules with at least twice the sample weight of tungstic oxide. Samples were loaded into an Isotope Cube elemental analyser (EA) and combusted at 1800 °C. The released gases were transported by helium through the EA to be separated. The $SO_2$ gas was carried into the Delta Plus XP isotope ratio mass spectrometer (ThermoFinnigan, Germany) via a conflo IV interface for determination of $^{32}S$ and $^{34}S$ (Table 3). The analytical precision is ±0.1 per mil. The sulfur isotope data are reported in the standard $\delta^{34}S$ notation in parts per thousand (‰) relative to the international Canyon Diablo Troilite (CDT) and were calculated by using the following equation (Table 3).

$$\delta^{34}S_{sample}(‰) = \left[\left(\ ^{34}S/\ ^{32}S\right)_{measured} / \left(\ ^{34}S/\ ^{32}S\right)_{VSMOW} - - 1\right] * 1000$$

**Table 3**
Stable oxygen and sulfur isotopic values for representative magnetite and pyrite, respectively, from massive magnetite ore in the Chahgaz mineral deposit.

| Series | Sample No. | Mineral | $\delta^{18}O$ ‰ SMOW | $\delta^{34}S$ ‰ CDT |
|---|---|---|---|---|
| 1 | M-001 | Magnetite | 6.32 | |
| 2 | M-002 | Magnetite | 2.99 | |
| 3 | M-003 | Magnetite | 2.49 | |
| 4 | M-004 | Magnetite | 2.64 | |
| 5 | M-005 | Magnetite | 2.18 | |
| 6 | Py-001 | Pyrite | | 23.96 |
| 7 | Py-002 | Pyrite | | 24.61 |
| 8 | Py-003 | Pyrite | | 24.94 |
| 9 | Py-004 | Pyrite | | 24.6 |
| 10 | Py-005 | Pyrite | | 22.54 |
| 11 | Py-006 | Pyrite | | 24.12 |
| 12 | Py-007 | Pyrite | | 23.79 |

## 4. Results

### 4.1. Host rocks

The major and trace element compositions of host rock samples distal to the ore bodies reported in Table 1 were used to classify the rocks and determine the tectonic setting at their time of formation. Photographs of representative samples are shown in Fig. 3 and representative photomicrographs in Fig. 4. The main rock types surrounding the Chahgaz deposit consist of felsic to intermediate subvolcanic rocks including granite to diorite and felsic volcanic rocks including rhyolite to rhyodacite, as well as mafic volcanic rocks including gabbro. The host rocks of the Chahgaz deposit were severely affected by *syn*-mineralization hydrothermal alteration and, therefore, immobile elements such as HFSE and their ratios were utilized for interpretation of tectonic setting of the rocks to reduce the effects of hydrothermal processes. The felsic to intermediate subvolcanic rocks mainly contain quartz, feldspars, plagioclase and minor biotite and exhibit a granular texture (Fig. 3a, b). The magmatic feldspars and plagioclase are increasingly replaced by actinolite and albite and minor calcite with proximity to the ore bodies. Primary plagioclase was replaced by chlorite, epidote, calcite and sericite (Fig. 4a). Granite contains abundant quartz and widespread tourmalinization, biotitization and carbonatization (Fig. 4b). The mafic subvolcanic rocks contain plagioclase, hornblende, biotite and lesser clinopyroxene (augite and diopside) as granular and intergranular phases (Fig. 3c). The primary magmatic minerals are variably replaced, primarily by actinolite, albite and epidote, as well as lesser sericite, calcite, phlogopite and magnetite in minor amounts with increasing proximity to the ore bodies. Sericitization and saussuritization of plagioclase crystals are commonly observed in the mafic rocks (Fig. 4c). Brown hornblende was variably replaced by secondary biotite, chlorite and tourmaline along the margin of the ore bodies (Fig. 4d).

The felsic to intermediate subvolcanic rocks plot within quartz diorite and syeno-diorite fields, and the mafic subvolcanic rocks plot within gabbro field on the total alkali vs. silica (TAS: Na2O + K2O vs. SiO2) discrimination diagram of Cox et al. (1979) (Fig. 5a). Felsic volcanic rocks are distinguished by the common occurrence of quartz, feldspar and plagioclase phenocrysts with highly silicic groundmass (Fig. 3d, e). Overgrowths of quartz and K-feldspar on primary plagioclase phenocrysts are common. The primary minerals are variably replaced by albite, sericite, actinolite, calcite, epidote, chlorite and magnetite (Fig. 4e). Later albitization, silicification and K-feldspatization increasingly affected these rocks with increasing proximity to magnetite-rich ore bodies. Supergene argillic alteration is partly developed overprinting other alteration types in outcrop and shallow samples. On the log($Zr/TiO_2$*0.0001) vs. log(Nb/Y) discrimination diagram of Winchester and Floyd (1977), felsic volcanic rocks are representative of rhyolite to rhyodacite (Fig. 5b). Rhyolite and rhyodacite often have porphyritic-granular and interstitial textures. Coarse-grained green

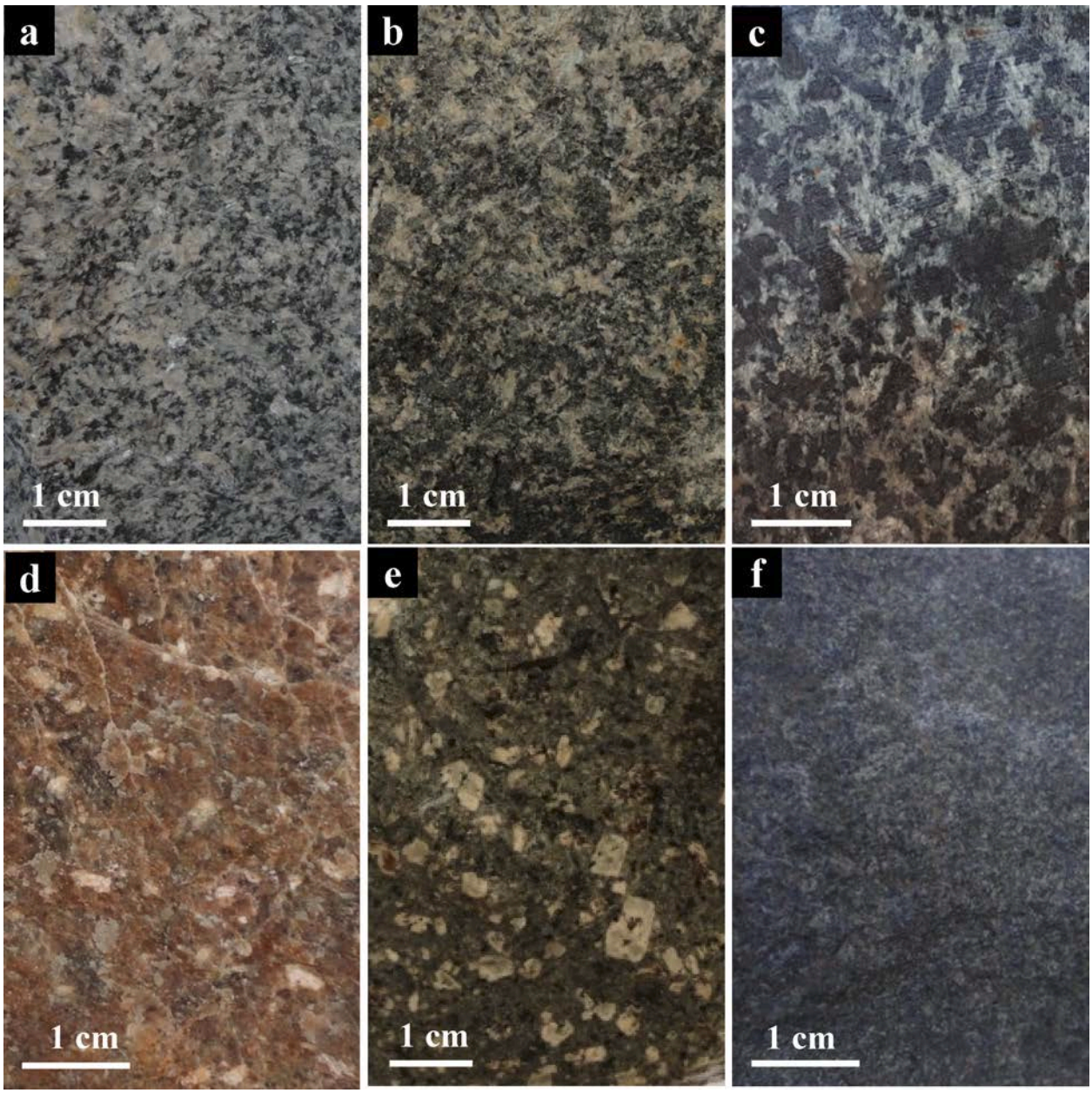


**Fig. 3.** Hand specimen photographs of all rock types from Chahgaz deposit. (a) Zarigan granite with secondary albite and quartz; (b) Diorite with less albitization and amphibolitization; (c) Gabbro with silicification; (d) Rhyolite with abundant secondary albite and quartz; (e) Rhyodacite with porphyry texture; (f) Dark green diabase with less amphibolitization. (For interpretation of the references to color in this figure legend, the reader is referred to the web version of this article.)

rocks are developed proximally to the ore bodies and are composed of coarse actinolite and pink albite grains.

Dark green diabase dikes crosscut other rock types and are mainly composed of plagioclase and amphibole, as well as minor biotite and magnetite (Figs. 3f and 4f). On the log($Zr/TiO_2$*0.0001) vs. log(Nb/Y) (Winchester and Floyd, 1977), diabase dikes lie within the sub-alkaline basalt field (Fig. 5c). On the log(Th) vs. Co diagram of Hastie et al. (2007), all samples exhibit calc-alkaline and high-K calc-alkaline affinities (Fig. 5d). On the Th/Hf vs. Ta/Hf geotectonic discrimination diagram of Schandl and Gorton (2002), the felsic volcanic rocks plot in active continental margin field (Fig. 5e). On the log(Ce/Nb) vs. log(Th/Nb) plot of Saunders and Tarnery (1991), all the mafic rocks including diabase dikes and gabbro plot predominantly within the field of back-arc basin basalts, except for one sample of diabase (Fig. 5f).

### 4.2. Hydrothermal alteration and mineralization

The host rocks of the Chahgaz deposit were affected by *syn*-mineralization hydrothermal alteration, which is characteristic of all mineral deposits in the Bafq district. The hydrothermal alteration assemblages are evidence of an important metasomatic component in the ore-forming process, commonly controlled by the chemical composition of the host rocks and mineralizing fluids, pressure and temperature (Reed, 1997; Meinert et al., 2005). The paragenetic sequence of hydrothermal alteration and mineralization in the Chahgaz deposit was determined based on field observation of mineralized outcrops, drill core logging, optical microscopic studies, and FE-SEM and EPMA analyses of representative mineralized samples (Fig. 6). The hydrothermal alteration assemblages associated with the Chahgaz iron mineralization include sodic-calcic, potassic, magnesium, silicic, sericitic, argillic and carbonatization, each of which varies according to the nature of the host rocks. The wall

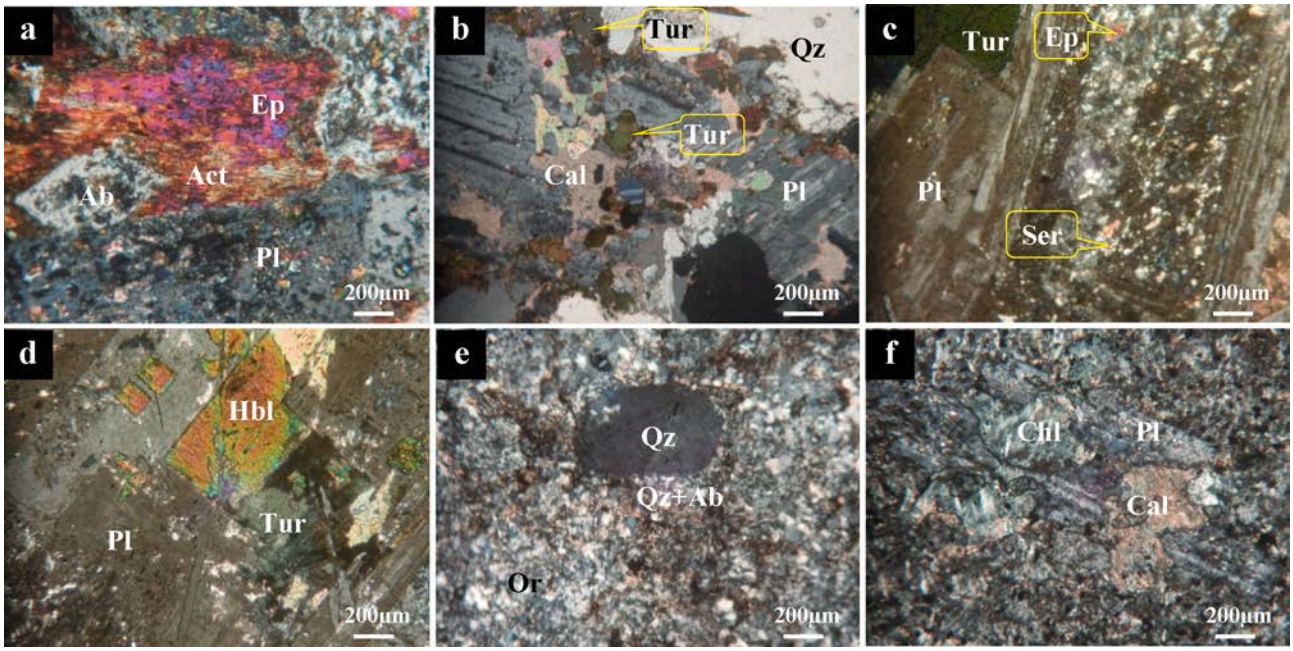


**Fig. 4.** Photomicrographs (XPL) showing altered rock types in Chahgaz deposit rocks. (a) Magmatic plagioclase is altered to actinolite, albite and epidote in diorite; (b) Granite with widespread tourmalinization and carbonatization; (c) saussuritization of magmatic plagioclase in hornblende gabbro; (d) Replacement of hornblende by tourmaline in hornblende gabbro; (e) overgrowth of albite and quartz around earlier quartz phenocryst in rhyolite; (f) Carbonatization and chloritization in diabase. All abbreviations after Whitney and Evans (2010): ab = albite, act = actinolite, cal = calcite, chl = chlorite, ep = epidote, hbl = hornblende, or = orthoclase, pl = plagioclase, qz = quartz, ser = sericite, tur = tourmaline.

rocks are pervasively altered by extensive sodic-calcic alteration characterized by the assemblage actinolite and albite. Potassic alteration is marked by K-feldspar as a late-stage phase that partially replaced albite grains, as well as sericitization. Magnesium alteration occurs locally along the faults and is characterized mainly by the assemblage serpentine and talc. Silicic alteration occurs after sodic and calcic alteration. Sericitic and argillic alteration formed both during and after sodic and calcic alteration. Carbonatization is the final hydrothermal alteration event in the deposit.

### 4.3. Magnetite and apatite mineralization

Magnetite mineralization occurs mainly as two massive magnetite-dominated ore bodies, and minor magnetite in magnetite-apatite veins and veinlets that crosscut the ore bodies and altered host rocks. Magnetite ore is dominated by massive magnetite that comprises ≥95% volume percent of the ore bodies, along with minor hematite, and rare rutile, titanite, apatite, allanite, siderite and ankerite, with late-stage calcite and hematite filling open spaces that resemble miarolitic or amygdaloidal cavities (Fig. 7a). Martitization of primary magnetite is observed in samples from stratigraphically higher, near-surface levels of the ore bodies. Modally minor primary hematite is also found in late-stage carbonate veinlets (Fig. 7b), but most hematite is secondary in origin as a result of oxidation of primary magnetite (Fig. 7c). The ore bodies with the sub-vertical shape have discordant structure-faulted contacts with their host rocks. The marginal zones of the massive magnetite ore bodies are mostly brecciated and display cataclastic texture. Additionally, disseminated magnetite (Fig. 7d) and veinlets of calcite ± magnetite ± apatite ± actinolite ± albite ± pyrite ± rutile ± titanite ± thorite are present within the altered host rocks and the massive magnetite ore.

Microscopic observations reveal a paragenetic sequence containing three generations of magnetite in the Chahgaz ore bodies. The early stage is a porous magnetite (Mag1) that comprises ≥95 vol% of the massive ore bodies. Triple junctions with 120° interfacial angles are observed among Mag1 grains (Fig. 7g). The massive magnetite ore bodies are dominated by Mag1 that locally preserve lava-like textures (massive, vesicular, miarolitic cavities and minor bladed magnetite) similar to those described for the El Laco IOA deposit, Chile (Park, 1961; Rhodes et al., 1999; Naslund et al., 2002; Tornos et al., 2016; Ovalle et al., 2018; Childress et al., 2020b) and other IOA deposits in the Chilean iron belt (Palma et al., 2020). The second generation of magnetite (Mag2) is present in veinlets accompanied by carbonate and minor apatite, quartz, titanite and thorite. The third generation of magnetite (Mag3) is modally very minor and occurs as micro granular magnetite in veinlets cutting massive magnetite and altered host rocks. All three magnetite generations do not display any zonation, exsolution texture or signs of alteration as revealed by examination using back-scattered electron (BSE) imaging.

Pyrite is present as disseminated grains within massive magnetite and in veinlets and late-stage fractures that crosscut Mag1 along with minor subhedral to anhedral pyrite that grew in cavities in Mag1 (Fig. 7h, i), similar to observations of late-stage pyrite reported for the Los Colorados (Reich et al., 2016; Deditius et al., 2018) and El Romeral (Rojas et al., 2018b) IOA deposits in the Chilean iron belt.

Apatite in the Chahgaz ore body occurs in trace amount as disseminated grains within the massive magnetite ore bodies, and with the assemblage carbonate (calcite and dolomite) ± apatite ± quartz ± thorite ± magnetite veinlets that crosscut the massive ore bodies (Fig. 7e), as well as apatite ± magnetite ± thorite ± zircon ± xenotime veinlets and disseminated apatite in the immediate altered host rocks (Fig. 7f). The Chahgaz magnetite ore bodies contain less apatite than other IOA deposits in the Bafq district (e.g., Torab and Lehmann, 2007; Jami et al., 2007).

### 4.4. Sodic-calcic alteration

Pervasive sodic-calcic alteration is distinguished in various host rocks and occurs both proximal and distal to the ore body. The sodic-calcic alteration is characterized by amphibole, albite and clinopyroxene, as well as K-feldspar and quartz in minor amounts (Fig. 8a, b). This alteration occurs either as massive altered bodies (green rock) or as

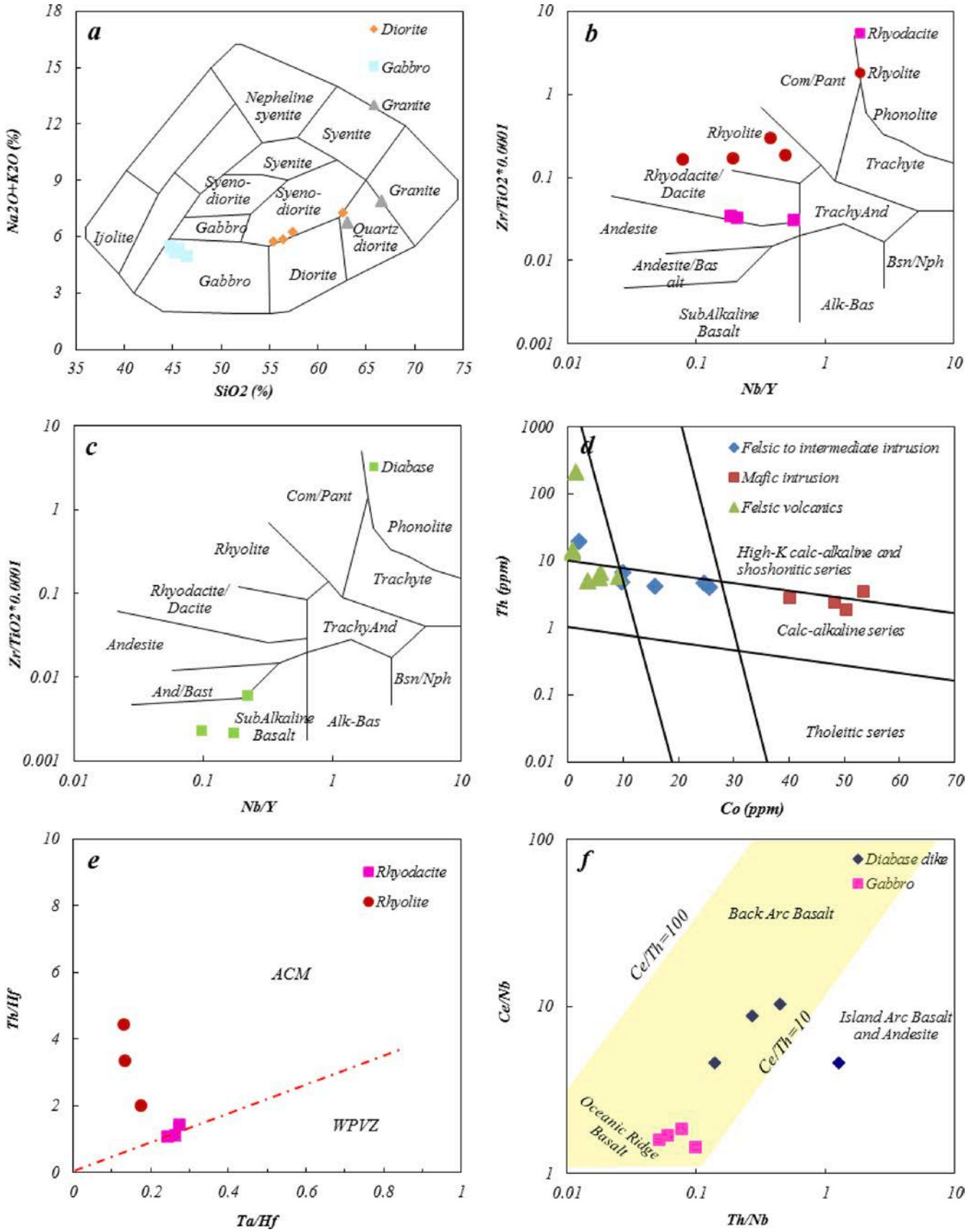


**Fig. 5.** Plots of Chahgaz (a) subvolcanic host rocks in TAS (Total alkali versus silica) diagram, (b, c) felsic volcanic host rocks and diabase dikes in log($Zr/TiO_2$*0.0001) vs. log($SiO_2$) discrimination diagram of Winchester and Floyd (1977), (d) rocks in log(Th) vs Co diagram of Hastie et al. (2007), (e) felsic volcanic rocks in Th/Hf vs. Ta/Hf diagram of Schandl and Gorton (2002), (f) mafic rocks in log(Ce/Nb) vs. log(Th/Nb) diagram of Saunders and Tarney (1991).

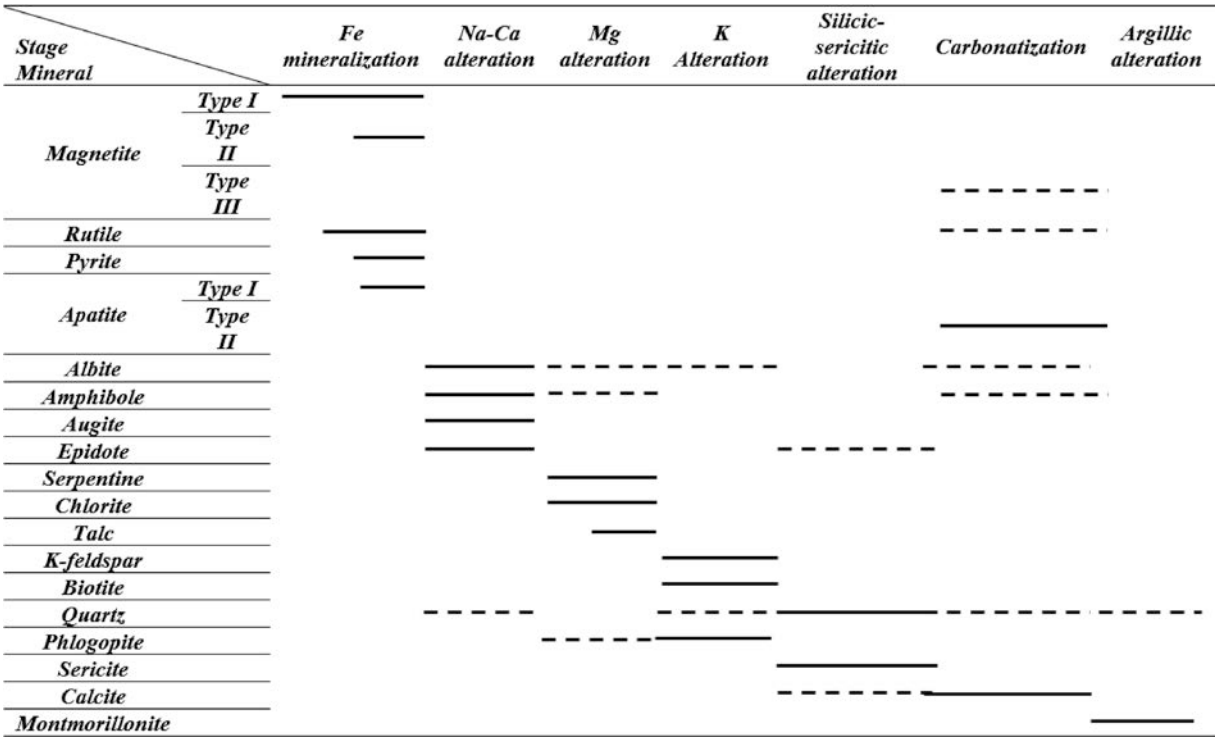


**Fig. 6.** Paragenetic sequence of ore minerals and the associated alteration assemblage in the Chahgaz mineral deposit (solid line: major phase; dash line: minor phase).

disseminated albite and amphibole in the host rocks (Fig. 4a). Amphibole is euhedral to subhedral and occurs mainly as elongate crystals with strong single-set parallel cleavages (Fig. 8a, b). Albite commonly occurs as anhedral to subhedral crystals that exhibit chessboard texture and white to pink color. Albite and amphibole also occur as patches in the altered host rocks. The recognition of the precursor rock composition, especially in the vicinity of mineralization zones, is commonly impossible due to the high intensity of the alteration. The EPMA analyses (Table 2) and nomenclature of Leake et al. (1997), the amphiboles in the Ca-Na alteration zone belong to the calcic group and fall in the actinolite and tremolite fields (Fig. 9a). Following the nomenclature of Morimoto et al. (1989), the EPMA analyses (Table 2) indicate that pyroxenes belong to Ca-rich pyroxene are in the augite field (Fig. 9b).

### 4.5. Magnesium alteration

Magnesium alteration is distinguished by serpentine and chlorite replacing earlier minerals, developed locally along the fault contacts in the country rocks (Fig. 8c). Serpentine is increasingly replaced by talc (Fig. 8d). The Mg-alteration assemblage consists of serpentine, chlorite and talc, as well as minor quartz, albite, phlogopite and K-feldspar. Magnesium alteration may be the consequence of hydrothermal fluids that interacted with dolomites belonging to the ECVSS.

### 4.6. Potassic alteration

Potassic alteration is partly superimposed on the sodic-calcic alteration, and locally occurs in the host rocks. Potassic alteration is represented by newly formed fine- to coarse-grained K-feldspar and minor phlogopite replacing secondary albite and pyroxene, as well as overgrowths on plagioclase and groundmass in the host rocks (Fig. 8e–g). The diabase dikes and gabbro are mainly composed of plagioclase and chloritized amphibole, and later formed biotite and K-feldspar resulting from potassic alteration.

### 4.7. Silicic and sericitic alteration

The Chahgaz ore-forming system proceeds with lower temperature sericitic and silicic alteration at higher stratigraphic levels of the ore bodies (Figs. 4c and 8h). Sericitic and silicic alterations overprint earlier sodic-calcic and potassic alteration assemblages, affecting all host rocks in the uppermost portion of the system. Sericitic alteration manifests as the assemblage sericite and chlorite that partly replaced secondary albite, which formed during sodic-calcic alteration, as well as primary minerals in the host rocks (Fig. 8e). Silicic alteration is represented by fine-grained quartz overgrowths on primary quartz, albite and K-feldspar in the host rocks, as well as secondary albite, K-feldspar and amphibole in alteration zones.

### 4.8. Late carbonatization and argillic alteration

Carbonatization was the final stage of alteration in the evolution of the ore system and variably affected all rock types and overprinted earlier alteration types throughout the deposit. Calcite veinlets occur in the altered host rocks and ore bodies (Fig. 8h). Additionally, calcite replaced primary feldspar and plagioclase in diorite, gabbro and diabase dikes (Fig. 8g). The host rocks are also overprinted by advanced argillic alteration characterized by montmorillonite and quartz that are present adjacent to faults at surface and shallow depths. In the argillic zone, albite (primary and secondary) and secondary K-feldspar were replaced by montmorillonite and chlorite (Fig. 8i). Quartz is unaltered in the argillic zone.

## 5. Magnetite chemistry

Compositional data for the three generations of magnetite (Mag1, Mag2 and Mag3) are reported in Table 2. Late-stage Mag3 is modally very minor and only one grain was analyzed by EPMA. The data reveal that Mag1 contains 3127–8090 ppm V (median: 4282 ppm V) and 150–39496 ppm Ti (median: 8402 ppm Ti). The data reveal that Mag2

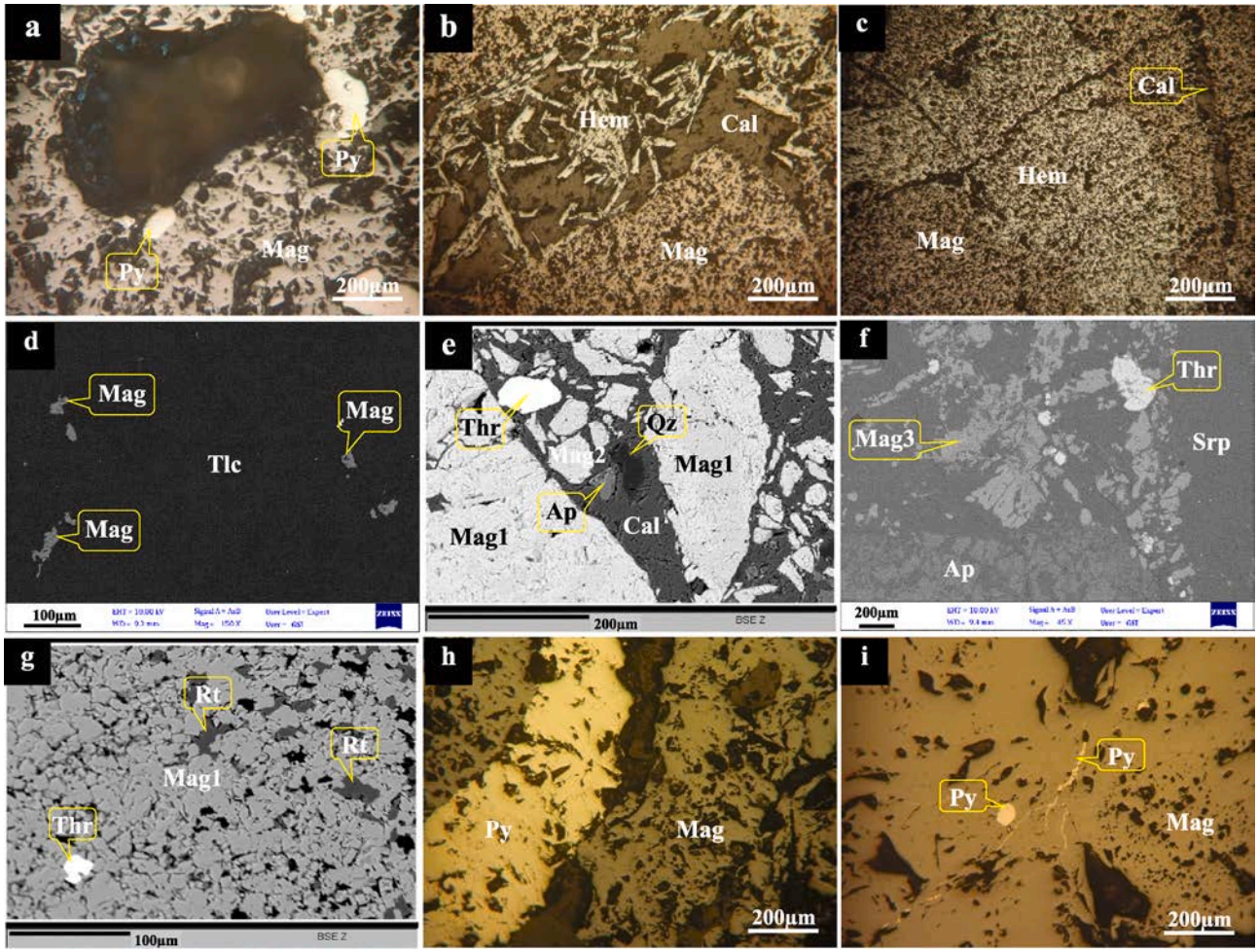


**Fig. 7.** Photomicrographs and SEM- and EPMA-backscattered electron (SEM-BSE and EPMA-BSE) images showing (a) miarolitic texture in massive magnetite, (b) calcite and primary hematite filled spaces in massive ore, (c) Hematite as a product of martitization, (d) disseminated magnetite within Mg-alteration zone, (e) apatite ± calcite ± Mag2 veinlets in massive magnetite (two types of magnetite1) with cataclastic texture, (f) apatite occurs as veinlet with thorite and magnetite within Mg-alteration zone, (g) magnetite with triple-junctions associated with minor rutile, (h) pyrite have filled micro-fractures within massive magnetite, (i) paragenesis of magnetite and pyrite. Abbreviations: ap = apatite, cal = calcite, hem = hematite, mag = magnetite, py = pyrite, qz = quartz, rt = rutile, srp = serpentine, thr = thorite, tlc = talc.

contains 2447–7138 ppm V (median: 3593 ppm V) and 60–27689 ppm Ti (median: 1703 ppm Ti). The analyzed point of Mag3 contains 135 ppm V and 400 ppm Ti.

## 6. Stable isotope geochemistry

Stable oxygen ($\delta^{18}O$) and sulfur ($\delta^{34}S$) isotopic data are presented in Table 3. The $\delta^{18}O$ values for Mag1 range from 2.2‰ to 6.3‰ (Table 3; Fig. 11a). Oxygen isotope abundances of Mag2 and Mag3 were not determined. The $\delta^{34}S$ values for pyrite samples coeval with Mag1 range from 22.54 to 24.94‰ (Table 3, Fig. 11b).

## 7. Discussion

### 7.1. Magnetite stable oxygen isotope and minor element concentrations

The $\delta^{18}O$ values reported here for magnetite from the Chahgaz deposit are similar to values reported for other IOA deposits in the Bafq district. Shamsipour et al. (2008) reported $\delta^{18}O$ values that vary from −0.64 to 2.19‰ for massive magnetite from the Chadormalu IOA deposit. Moore and Modabberi (2003) reported $\delta^{18}O$ values between 3.66 and 4.38‰ for massive magnetite samples from the Choghart IOA deposit. Mehdipour et al. (2019) reported $\delta^{18}O$ values ranging from 4.44 to 5.27‰, 2.87 to 4.22‰ and 3.18 to 4.12‰ for massive magnetite from the Choghart, Chadormalu and Se-Chahun IOA deposits, respectively. The authors of the aforementioned studies of IOA deposits in the Bafq district interpreted their reported $\delta^{18}O$ values to indicate a magmatic source reservoir for oxygen in magnetite.

The $\delta^{18}O$ values reported here for magnetite from the Chahgaz IOA deposit are shown in Fig. 11a along with published ranges for $\delta^{18}O$ values for magnetite from other well known IOA deposits such as El Laco (Chile), Kiruna (Sweden) and Bafq district (Iran). All but one of the $\delta^{18}O$ values for magnetite from the Chahgaz IOA deposit plot within the range of 1.0 to 4.0‰ determined by Taylor (1967) for igneous magnetite; i.e., magnetite that crystallized from silicate melt or from magmatic-hydrothermal fluid evolved from silicate melt. Troll et al. (2019) reported a more extensive set of $\delta^{18}O$ values for magnetite from IOA deposits globally that extends the range of $\delta^{18}O$ values from 0.0 to 7.0‰. Using this extended range from Troll et al. (2019), all of the $\delta^{18}O$ values for magnetite from Chahgaz are consistent with an origin from silicate melt and/or magmatic-hydrothermal fluid. The elevated $\delta^{18}O$ value of 6.32‰ for one sample of Mag1 from Chahgaz is consistent with similarly elevated values of 7.0‰ and 6.7‰ reported by Childress et al. (2016) for massive magnetite from the Pea Ridge and Pilot Knob IOA deposits, Missouri, respectively, and by Rodriguez-Mustafa et al. (2020) for massive magnetite from the Quince IOA prospect, Chile. Childress et al.

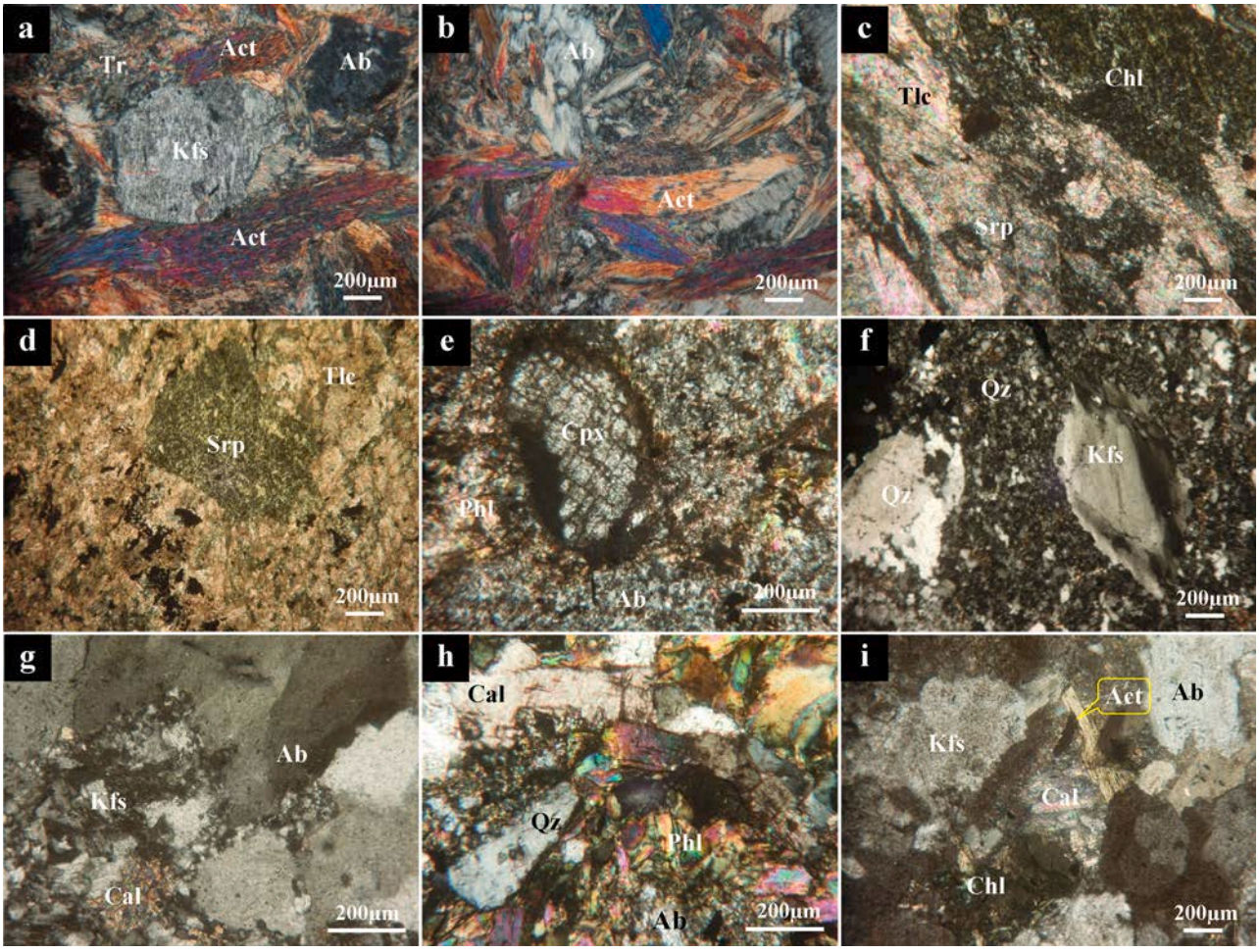


**Fig. 8.** Photomicrographs showing characteristic features of metasomatic zones, all in XPL. (a) Metasomatic actinolite and albite in Na-Ca alteration and metasomatic k-feldspar overprinted albite; (b) Actinolite replacing earlier albite; (c) Chlorite and serpentine replacing earlier minerals, and later replacement of serpentine by talc in magnesium alteration; (d) Replacement of serpentine by talc in magnesium alteration, talc is altering to clay mineral; (e) Phlogopite replacing earlier albite and clinopyroxene; (f) Newly formed K-feldspar crystals in quartz-rich groundmass in potassic alteration; (g) Overgrowth of fine-rained K-feldspar and calcite on earlier albite; (h) Replacement of albite by phlogopite; calcite veinlet and newly formed quartz in silicification and carbonatization alteration; (i) argillic alteration of K-feldspar and metasomatic albite. Abbreviations: ab = albite, act = actinolite, cal = calcite, chl = chlorite, cpx = clinopyroxene, kfs = k-feldspar, phl = phlogopite, qz = quartz, srp = serpentine, tr = tremolite, tlc = talc.

(2016), Troll et al. (2019) and Rodriguez-Mustafa et al. (2020) concluded that the $\delta^{18}O$ values for magnetite in each of their studies indicate that oxygen in magnetite was sourced from silicate magma. Those three studies also reported $\delta^{56}Fe$ values for the same magnetite samples that are consistent with a silicate magma source for iron in magnetite. We do not have iron isotopic data for magnetite samples from the Chahgaz IOA deposit. However, based on the comparison of $\delta^{18}O$ values for samples from Chahgaz with magnetite from other well studied IOA deposits in the Bafq district and globally, we conclude that oxygen in magnetite from the Chahgaz deposit was sourced from silicate magma.

The concentrations of V and Ti in magnetite from the Chahgaz deposit are plotted in Fig. 10a along with fields that distinguish magnetite from hydrothermal and igneous origins as determined by Nadoll et al. (2014). The V and Ti concentrations (Fig. 10a) are consistent with magnetite crystallized from silicate melt or from high-temperature magmatic-hydrothermal fluid. The concentrations of Cr and V in magnetite from the Chahgaz deposit are plotted in Fig. 10b along with fields that distinguish magnetite from Fe-Ti, V mineral deposits, porphyry deposits, Kiruna IOA deposits, and iron oxide-copper-gold (IOCG) deposits as determined by Dupuis and Beaudoin (2011), Nadoll et al. (2014) and Knipping et al. (2015b). There is agreement in the literature that magnetite in Fe-Ti, V mineral deposits crystallized from silicate melt, and magnetite in porphyry deposits crystallized from hypogene magmatic-hydrothermal fluid (cf. Boudreau and Simon, 2007; Bilenker et al., 2017; Driscoll and VanTongeren, 2017). There is significant debate about the genesis of Kiruna-type IOA deposits. Genetic models for the formation of Kiruna-type deposits include formation by meteoric or metamorphic hydrothermal fluids that scavenge metals from intermediate to mafic host rocks (Menard, 1995; Rhodes and Oreskes, 1999; Barton and Johnson, 1996; Barton and Johnson, 2004; Haynes et al., 1995; Rhodes et al., 1999; Haynes, 2000; Sillitoe and Burrows, 2002; Dare et al., 2015), and magmatic-hydrothermal fluids that scavenge metals directly from magma (Pollard, 2006; Westhues et al., 2016, 2017a, 2017b). A non-hydrothermal genetic model proposes that Kiruna-type IOA deposits form by a purely igneous process wherein a parent silicate melt of intermediate to mafic composition separates into immiscible Si-rich, Fe-P-poor melt and conjugate Fe-P-rich, Si-poor melt, followed by coalescence and physical separation of the Fe-P-rich melt to form an iron oxide – apatite ore body (Park, 1961; Nyström and Henríquez, 1994; Travisany et al., 1995; Naslund et al., 2002; Henríquez et al., 2003; Chen et al., 2010; Tornos et al., 2016, 2017; Velasco et al., 2016; Hou et al., 2018). In the case of IOCG deposits, there is agreement in the literature that magnetite precipitates from hydrothermal fluid, but there is a lack of consensus for the origin of the mineralizing fluid, with hypotheses that invoke magmatic-hydrothermal fluid (e.g., Childress

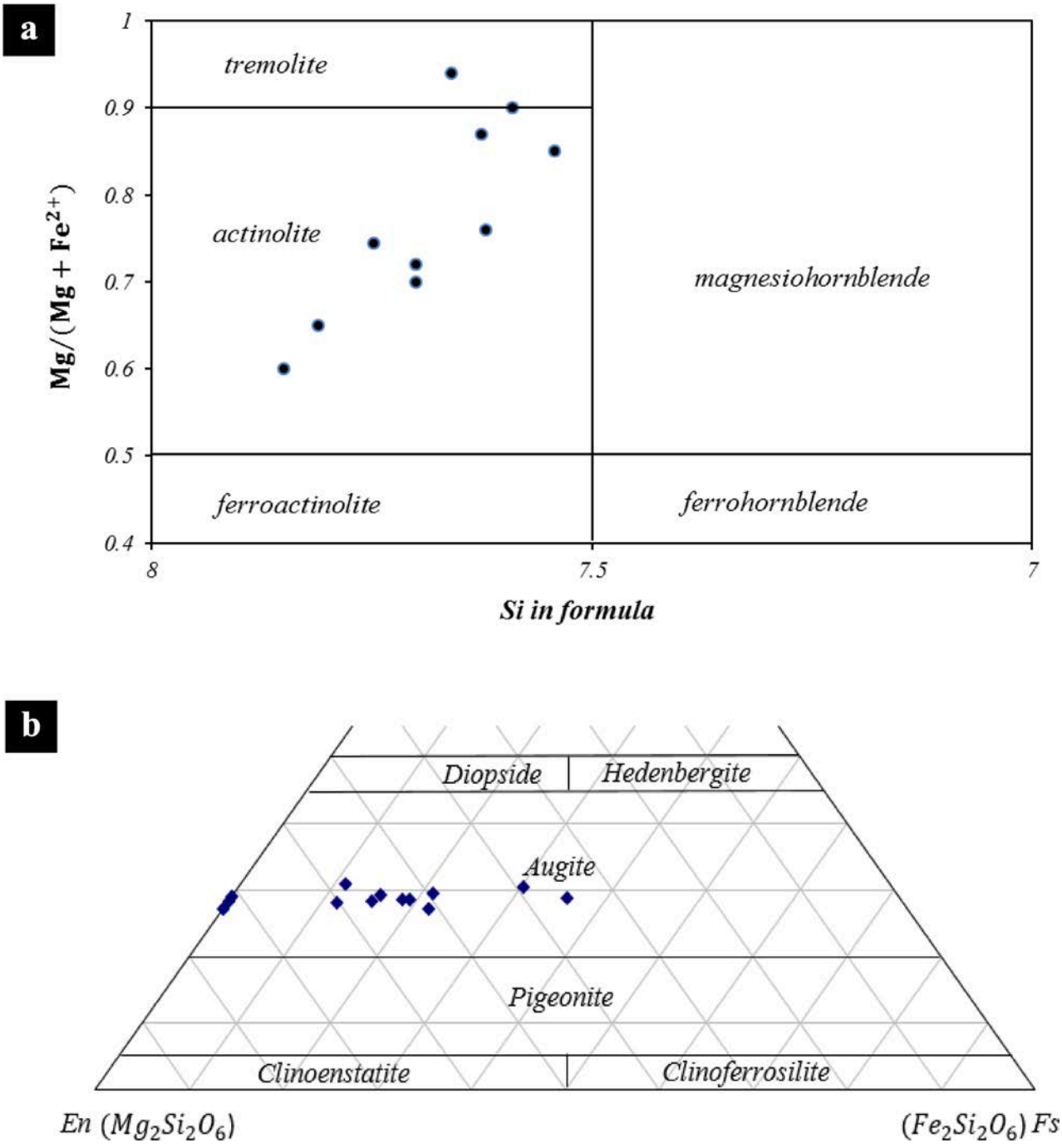


**Fig. 9.** (a) Classification of the Ca-rich pyroxene; (b) calcic amphiboles in the metasomatic zones of the Chahgaz deposit.

et al., 2020a; Rodriguez-Mustafa et al., 2020), and basinal brine (cf. Barton and Johnson, 1996).

Interestingly, none of the magnetite samples from Chahgaz plot in the Kiruna field on Fig. 10b, which is similar to data reported for magnetite from the IOA deposit throughout the Cretaceous iron belt of northern Chile (Knipping et al., 2015a, 2015b; Deditius et al., 2018; Palma et al., 2019, 2020; Salazar et al., 2020) and the Plio-Pleistocene El Laco IOA deposit, Chile (Ovalle et al., 2018; La Cruz et al., 2020). Those three studies concluded that the V and Cr concentrations of magnetite, along with a larger set of minor element concentration data for magnetite, are consistent with an origin by precipitation from high-temperature magmatic-hydrothermal fluid, which is consistent with oxygen (including Δ17O) and $\delta^2$H values reported for magnetite from El Laco (Childress et al., 2020b) and iron isotope data for magnetite presented by those authors. The conclusions of those studies build on the work of Dare et al. (2014), Dare et al. (2015) who reported a large set of minor and trace element data for magnetite from the El Laco IOA deposit and interpreted the data to indicate that the ore bodies formed by hypogene hydrothermal processes, and not liquid immiscibility.

Childress et al. (2020b) used their reported $\delta^{18}$O values for magnetite from El Laco to test the liquid immiscibility hypothesis and reported that the hypothesis fails when evaluating the oxygen isotope data using experimentally constrained partitioning data for oxygen isotopes between immiscible Si-rich, Fe-P-poor melt and conjugate Fe-P-rich, Si-poor melt. Those experimental data from Kyser et al. (1998) require that the Si-rich, Fe-poor melt has the same $\delta^{18}$O value as the conjugate Fe-rich, Si-poor melt that crystallizes magnetite to form an IOA ore body. In the case of the Chahgaz IOA deposit, there are no published oxygen

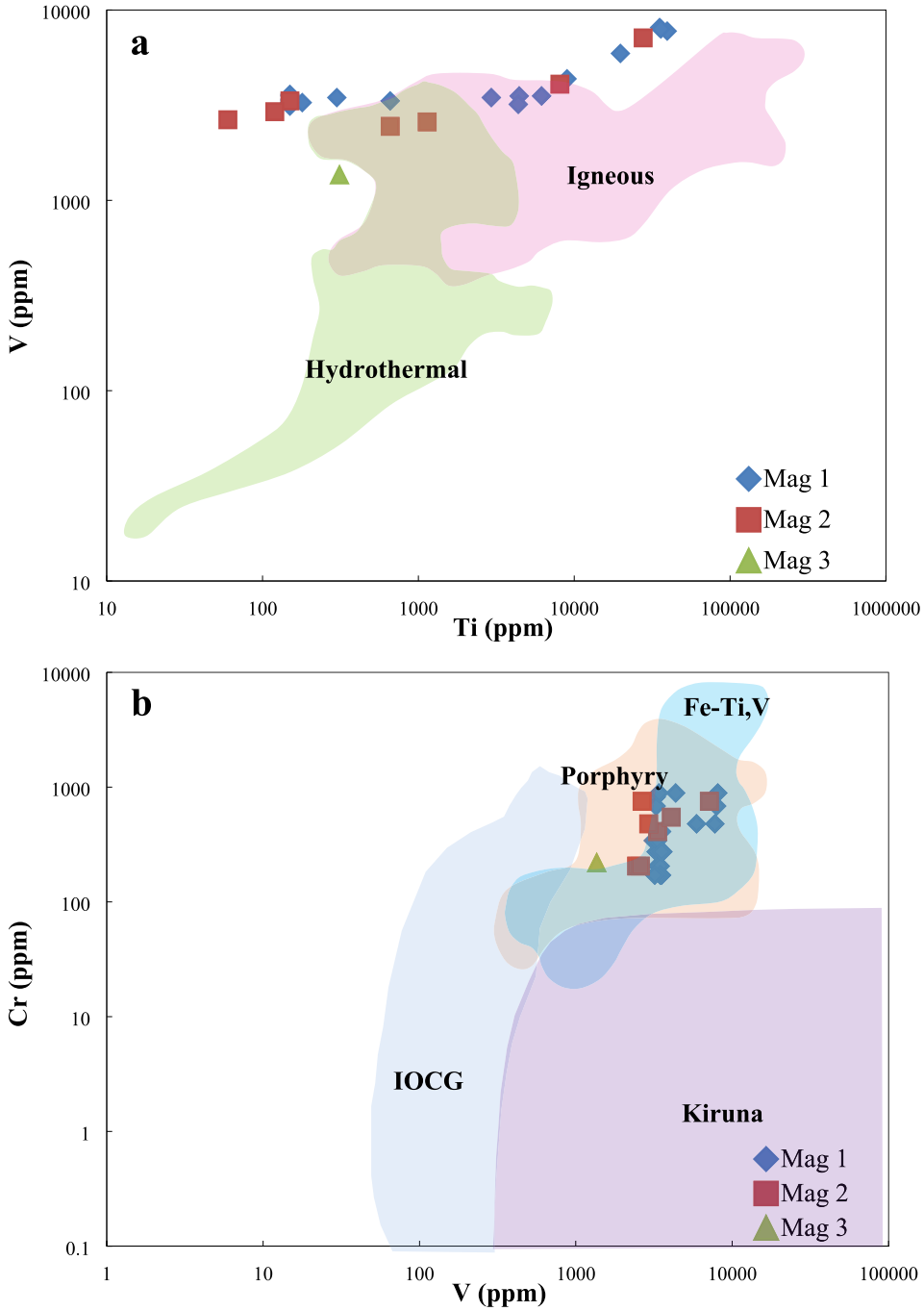


**Fig. 10.** (a) V vs. Ti concentrations (in ppm) and (b) Cr vs. V concentrations (in ppm) in all generations of magnetite from the Chahgaz deposit. Diagram and fields from Nadoll et al. (2015) and Knipping et al. (2015b).

isotope data for unaltered igneous host rocks that can be used to test the liquid immiscibility hypothesis. However, considering that the calc-alkaline igneous rocks in the Bafq district formed in a subduction zone analogous to the Andean margin, it is plausible to conclude that unaltered igneous host rocks in the Chahgaz deposit would have $\delta^{18}O$ values of ~7 to 9‰ if the ore bodies crystallized from Fe-rich melt that had been in equilibrium with conjugate andesitic melt. That the majority of $\delta^{18}O$ values for magnetite from the Chahgaz deposit are considerably lighter than 7 to 9‰ leads us to conclude that liquid immiscibility is not a plausible explanation for the deposit. This agrees with the observations of hydrothermal textures in the deposit discussed above and also experimental data for the Cl-free $SiO_2$-$TiO_2$-$Al_2O_3$-$Fe_2O_3$-FeO-MnO-MgO-$CaF_2$ system reported by Hou et al. (2018) that require an immiscible Fe-P-rich melt to contain 39 wt% $P_2O_5$ if the immiscible Fe-P-rich melt forms by liquid immiscibility from a parent silicate melt. The $P_2O_5$ content of the Chahgaz massive magnetite ranges from 0.006 to 0.568 wt%, with an average of 0.123 wt%, consistent with the low modal abundance of apatite in the Chahgaz ore bodies. The $P_2O_5$ content is two orders of magnitude less than Hou et al. (2018) reported is required to stabilize an immiscible Fe-P-rich melt. These data eliminate the possibility that the massive Chahgaz magnetite ore crystallized from an immiscible Fe-P-rich melt.

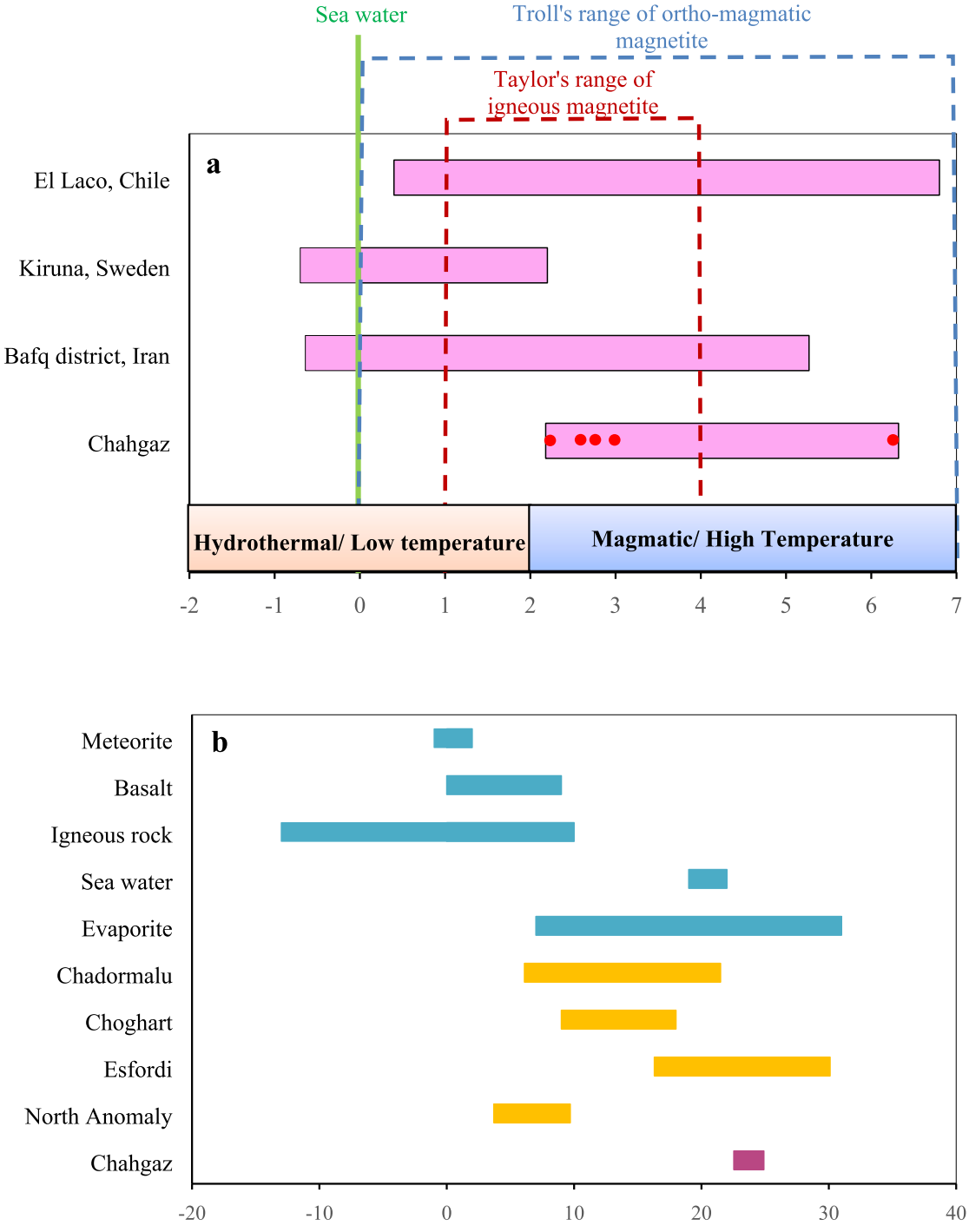


**Fig. 11.** (a) Oxygen isotope values for magnetite from Chahgaz massive ores compared to other IOA deposits; deposits in the Bafq district include: Choghart, Chadormalu and Se-Chahun. Values for El Laco from Rhodes and Oreskes (1999), Nyström et al. (2008), Tornos et al. (2016) and Childress et al. (2020b); data from those studies are not shown for samples where Δ17O and δ2H indicate minor to significant post-mineralization alteration. Values for Kiruna from Nyström et al. (2008) and Johnsson et al. (2013). Values for Bafq deposits from (Moore and Modabberi, 2003; Shamsipour et al., 2008; Mehdipour et al., 2019). (b) Sulfur isotope values for pyrite from Chahgaz massive ores compared to other IOA deposits in the Bafq district; a comparison is made to the main sulfur reservoirs (Hoefs, 2004) compared to pyrite from other IOA deposits in the Bafq district. Values for Chadormalu, Choghart, Esfordi and North Anomaly from Heidarian et al. (2017), Sadeghi Davati (2008), Jami (2005) and Sadeghi (2008), respectively.

### *7.2. Sulfur isotopes in pyrite*

The sulfur isotope data indicate that sulfur in pyrite, which is coeval with Mag1, was derived from a non-magmatic source. The $\delta^{34}S$ values for pyrite reported here are consistent with values of 16.3 to 30.1‰ reported by Jami (2005) for the Esfordi deposit, Bafq district. That author proposed an evaporitic source for sulfur, following Claypool et al. (1980). Sadeghi (2008) and Sadeghi Davati (2008) reported $\delta^{34}S$ values that range from 3.7 to 9.7‰ and 9 to 18‰ for pyrite from the North Anomaly and Choghart deposits, respectively. Heidarian et al. (2017) reported $\delta^{34}S$ values that range from 8.9 to 14.4‰ and 18.7 to 21.5‰ for massive- and vein-type magnetite-rich ores, respectively, in the Chadormalu IOA deposit, Bafq district. The $\delta^{34}S$ data reported here for pyrite from the Chahgaz deposit are consistent with published $\delta^{34}S$ data

reported for other Bafq IOA deposits and consistent with an evaporitic source for sulfur.

### 7.3. A genetic model for the formation of the Chahgaz IOA deposit

The $\delta^{18}O$ values reported here for massive magnetite Mag1, which comprises ≥95% of the Chahgaz ore bodies, indicate that oxygen was (Aghanabati, 2008) sourced from a silicate magma reservoir. The abundances of minor elements such as Cr, Ti and V in magnetite are consistent with the minor element compositions of magnetite in porphyry mineral deposits that formed unequivocally by precipitation from magmatic-hydrothermal fluid. The textures documented here for massive magnetite Mag1 are consistent with formation by a combination of hydrothermal and igneous processes. Based on a comparison of the data and observations reported here with those reported for other IOA deposits, we conclude that the magnetite flotation model proposed by Knipping et al. (2015a) explains the formation of the Chahgaz deposit. Briefly, that model invokes crystallization of magnetite from an intermediate composition silicate melt such as andesite, followed by exsolution of a magmatic-hydrothermal fluid from the melt where the fluid bubbles nucleate and grow on magnetite crystal faces and form a magnetite-fluid suspension. The magmatic-hydrothermal fluid will be enriched in iron, which partitions efficiently from the melt to the fluid as the soluble complex $FeCl_2$ (Simon et al., 2004). As the buoyant magnetite-(Fe-rich)-fluid suspension ascends along permeable structures such as faults in the superjacent environment, primary igneous magnetite continues to grow by sourcing iron from the cooling magmatic-hydrothermal fluid and deposition of magnetite in faults occurs when the proportion of magnetite in the suspension exceeds about 40 vol%, depending on the density (i.e., salinity) of the fluid (Knipping et al., 2015a, 2019). The systematically decreasing abundance of minor elements, e.g., Ti, in magnetite is consistent with progressive growth of primary igneous magnetite from a cooling magmatic-hydrothermal fluid. The model also explains the presence of vesicles within the massive Mag1 ore bodies. The Mag2 magnetite generation that is modally minor and present in veinlets that cut the massive Mag1 ore body, is plausibly the result of the local dissolution and reprecipitation of Mag1 by the mineralizing fluid. The $\delta^{34}S$ values of pyrite indicate that sulfur was introduced into the system from a non-magmatic source, plausibly from evaporites in the ECVSS. The $\delta^{34}S$ values for pyrite can be explained by assimilation of sulfur-bearing sedimentary rocks form the ECVSS into the primary silicate magma from which the ore fluid evolved.

## 8. Conclusions

The Chahgaz ore deposit is one of the largest IOA deposits identified in Bafq mining district in Iran. The deposit is hosted in calc-alkaline igneous rocks that range from granite to diorite and rhyolite to rhyodacite that are increasingly altered with proximity to the magnetite-rich ore bodies, and display replacement textures. The characteristics of the Chahgaz deposit are consistent with Kiruna-type iron oxide- apatite

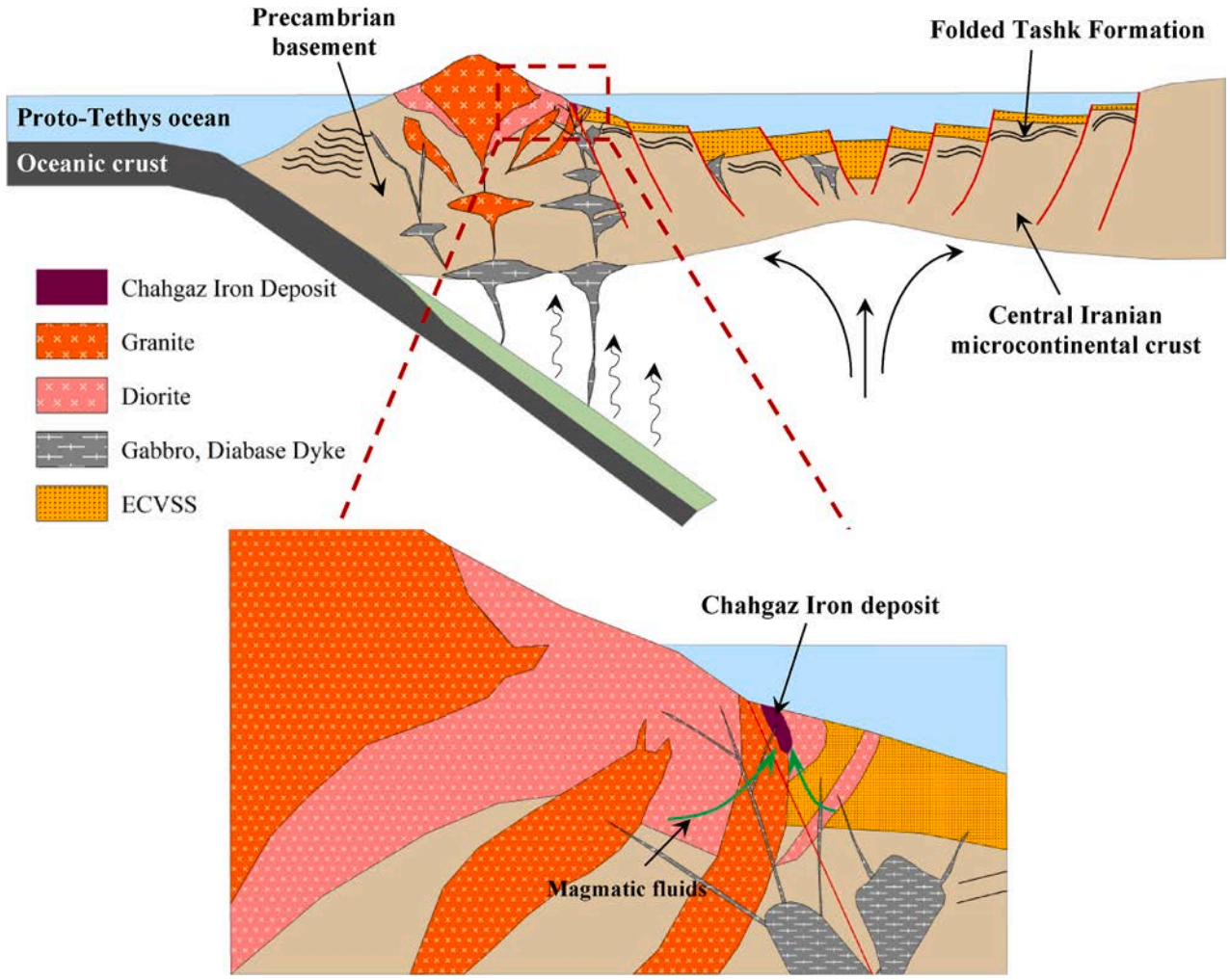


**Fig. 12.** A schematic model showing the relationship between magmatism and iron mineralization at Chahgaz deposit in Central Iran (modified from Rajabi et al., 2015).

(IOA) deposits globally, including (i) several types of hydrothermal alteration such as sodic-calcic, potassic, magnesium, silicic and carbonatization, (ii) calc-alkaline affinities of igneous rocks associated to mineralization, (iii) chemical composition of magnetite, and (iv) low sulfide contents of ores. The geochemical and tectonomagmatic investigations in this deposit indicate a calc-alkaline and active continental-margin arc setting for felsic host rocks in relation to subduction of Proto-Tethyan oceanic crust beneath the Central Iranian microcontinent in the Early Cambrian followed by emplacement of diabasic dykes in a back-arc basin (Fig. 12). Three generations of magnetite are present in the deposit, with the concentrations of minor elements overlapping those reported for magnetite from Fe-Ti, V deposits and porphyry deposits. The $\delta^{18}O$ values for magnetite indicate a silicate magma source reservoir for oxygen. The $\delta^{34}S$ values for pyrite paragenesis with Mag1 reveal magma contamination plausibly by assimilation of sulfur-bearing sedimentary rocks in the ECVSS. The data are consistent with initial growth of magnetite from silicate melt, subsequent degassing of the melt and formation of a magnetite-fluid suspension that ascended along faults to form the massive magnetite ore bodies. Decrease of oxygen fugacity and increase of sulfur fugacity during the magnetite crystallization finally led to deposition of pyrite in the late stage of magnetite crystallization. At the final stage of mineralization, magnetite grains deposited in the fractures of previous massive magnetites and alteration zones accompanied with calcite and quartz from a low-T hydrothermal fluid.

## Declaration of Competing Interest

The authors declare that they have no known competing financial interests or personal relationships that could have appeared to influence the work reported in this paper.

## Acknowledgements

This paper is part of Ph.D. thesis of the first author at the University of Tehran, Iran. This research was supported by the University of Tehran and Iran Minerals Production and Supply Company (IMPASCO), as well as Iranian Central Plateau Iron Ore Mines Company. ACS acknowledges funding from NSF EAR 1924142. The authors would like to thank Mr. Eslami and Mr. Mirabi for their field assistance.

## References

Aghanabati, A., 2008. In: Stratigraphy Encyclopedia of Iran: Precambrian to Silurian. Geological Survey of Iran, Tehran, Iran, p. 658.

Alavi, M., 1991. Tectonic map of the Middle East: Tehran, Geological Survey of Iran, scale 1:5,000,000.

Barton, M.D., 2014. Iron oxide (-Cu-Au-REE-P-Ag-U-Co) systems: In: Holland, H.D., Turekian, K.K. (Eds.), Treatise on Geochemistry Oxford. Elsevier, Second Edition 13, pp. 513–536. doi:10.1016/B978-0-08-095975-7.01123-2.

Barton, M.D., Johnson, D.A., 1996. Evaporitic source model for igneous related Fe oxide–(REE–Cu–Au–U) mineralization. Geology 24, 259–262. https://doi.org/10.1130/0091-7613(1996)024<0259:ESMFIR>2.3.CO;2.

Bilenker, L.B., Van Tongeren, J., Lundstrom, C.C., Simon, A.C., 2017. Iron isotopic evolution during fractional crystallization of the uppermost Bushveld Complex layered mafic intrusion. Geochem. Geophys. Geosyst. 18 (3), 956–972. https://doi.org/10.1002/2016GC006660.

Bilenker, L.D., Simon, A.C., Reich, M., Lundstrom, C.C., Gajos, N., Bindeman, I., Munizaga, R., 2016. Fe–O stable isotope pairs elucidate a high-temperature origin of Chilean iron oxide-apatite deposits. Geochim. Cosmochim. Acta 177, 94–104. https://doi.org/10.1016/j.gca.2016.01.009.

Borumandi, H., 1973. Petrographische und lagerstättenkunliche untersuchung der Esfordi- Formation zwischen Mishdovan und Kushk bei Bafq (Zentraliran), Diss. RWTH Aachen, 174 p.

Boudreau, A., Simon, A.C., 2007. Crystallization and degassing in the basement sill, McMurdo Dry Valleys, Antarctica. J. Petrol. 48 (7), 1369–1386. https://doi.org/10.1093/petrology/egm022.

Chen, H., Clark, A.H., Kyser, T.K., Ullrich, T.D., Baxter, R., Chen, Y., Moody, T.C., 2010. Evolution of the Giant Marcona-Mina Justa iron oxide-copper-gold district, South-Central Peru. Econ. Geol. 105, 155–185. https://doi.org/10.2113/gsecongeo.105.1.155.

Childress, T., Simon, A., Day, W.C., Lundstrom, C.C., Bindeman, I., 2016. Iron and oxygen isotope signatures of the Pea Ridge and Pilot Knob magnetite-apatite deposits, southeast Missouri, USA. Econ. Geol. 111 (8), 2033–2044. https://doi.org/10.2113/econgeo.111.8.2033.

Childress, T., Simon, A.C., Reich, M., Barra, F., Arce, M.J., Lundstrom, C., Bindeman, I., 2020a. Formation of the Mantoverde iron oxide-copper-gold (IOCG) deposit, Chile: Insights from Fe and O stable isotopes and comparisons to iron oxide-apatite (IOA) deposits. Miner. Deposita 55, 1489–1504. https://doi.org/10.1007/s00126-019-00936-x.

Childress, T., Simon, A.C., Reich, M., Barra, F., Bilenker, L.D., La Cruz, N., Bindeman, I. N., Ovalle, J.T., 2020b. Triple oxygen, hydrogen, and iron stable isotope signatures indicate a silicate magma source and magmatic-hydrothermal genesis for magnetite ore bodies at El Laco, Chile. Econ. Geol. 115 (7), 1519–1536. https://doi.org/10.5382/econgeo.4760.

Claypool, G., Holser, W., Kaplan, I., Sakai, H., Zak, I., 1980. The age curves of sulfur and oxygen isotopes in marine sulfate and their mutual interpretation. Chem. Geol. 28, 199–260. https://doi.org/10.1016/0009-2541(80)90047-9.

Daliran, F., 2002. Kiruna-type iron oxide-apatite ores and apatitites of the Bafq district, Iran, with an emphasis on the REE geochemistry of their apatites. In: Porter, T.M. (Ed.), Hydrothermal Iron Oxide Copper-Gold and Related Deposits: A Global Perspective. PGC Publishing Adelaide Australia 2, pp. 303–320.

Dare, S.A.S., Barnes, S.J., Beaudoin, G., Méric, J., Boutroy, E., Potvin-Doucet, C., 2014. Trace elements in magnetite as petrogenetic indicators. Miner. Deposita 49, 785–796. https://doi.org/10.1007/s00126-014-0529-0.

Dare, S.A., Barnes, S.J., Beaudoin, G., 2015. Did the massive magnetite "lava flows" of El Laco (Chile) form by magmatic or hydrothermal processes? New constraints from magnetite composition by LA-ICP-MS. Miner. Deposita 50 (5), 607–617. https://doi.org/10.1007/s00126-014-0560-1.

Deditius, A.P., Reich, M., Simon, A.C., Suvorova, A., Knipping, J., Roberts, M.P., Saunders, M., 2018. Nanogeochemistry of hydrothermal magnetite. Contrib. Mineral. Petrol. 173 (6), 46. https://doi.org/10.1007/s00410-018-1474-1.

Driscoll, B., VanTongeren, J.A., 2017. Layered intrusions: from petrological paradigms to precious metal repositories. Elements 13 (6), 383–389. https://doi.org/10.2138/gselements.13.6.383.

Dupuis, C., Beaudoin, G., 2011. Discriminant diagrams for iron oxide trace element fingerprinting of mineral deposit types. Miner. Deposita 46 (4), 319–335. https://doi.org/10.1007/s00126-011-0334-y.

Förster, H., Jafarzadeh, A., 1994. The Bafq mining district in Central Iran: a highly mineralized Infracambrian volcanic field. Econ. Geol. 89, 1697–1721. https://doi.org/10.2113/gsecongeo.89.8.1697.

Grassineau, N.V., Mattey, D.P., Lowry, D., 2001. Sulfur isotope analysis of sulfide and sulfate minerals by continuous flow-isotope ratio mass spectrometry. Anal. Chem. 73, 220–225. https://doi.org/10.1021/ac000550f.

Groves, D.I., Bierlein, F.P., Meinert, L.D., Hitzman, M.W., 2010. Iron oxide copper-gold (IOCG) deposits through earth history: implication for origin, lithospheric setting, and distinction from other epigenetic iron oxide deposits. Econ. Geol. 105, 641–654. https://doi.org/10.2113/gsecongeo.105.3.641.

Haghipour, A., Pelissier, G., 1977. Geology of the Saghand Sector. In: Haghipour, A., Valeh, N., Pelissier, G., Davoudzadeh, M. (Eds.), Explanatory Text of the Ardekan Quadrangle Map. Geological Survey of Iran, 8, 10-68.

Haghipour, A., Aghanabati, A., 1989. Geological map of Iran. geological survey of Iran, Tehran, Scale 1:2,500,000.

Hastie, A.R., Kerr, A.C., Pearce, J.A., Mitchell, S.F., 2007. Classification of altered volcanic island arc rocks using immobile trace elements: development of the Th-Co discrimination diagram. J. Petrol. 48, 2341–2357. https://doi.org/10.1093/petrology/egm062.

Haynes, D.W., 2000. Iron oxide copper (-gold) deposits: their position in the ore deposit spectrum and modes of origin. In: Porter, T.M. (Ed.), Hydrothermal Iron Oxide Copper-Gold and Related Deposits: A Global Perspective, Australian Mineral Foundation, Adelaide, PGC Publishing, pp. 71–90.

Haynes, D.W., Cross, K.C., Bills, R.T., Reed, M.H., 1995. Olympic Dam ore genesis: a fluid-mixing model. Econ. Geol. 90 (2), 281–307. https://doi.org/10.2113/gsecongeo.90.2.281.

Henríquez, F., Naslund, H.R., Nyström, J.O., Vivallo, W., Aguirre, R., Dobbs, F.M., Lledo, H., 2003. New field evidence bearing on the origin of the El Laco magnetite deposit, Northern Chile-a discussion. Econ. Geol. 98 (7), 1497–1500. https://doi.org/10.2113/gsecongeo.98.7.1497.

Hitzman, M.W., 2000. Iron oxide-Cu-Au deposits: what, where, when, and why. In: Porter, T.M. (Ed.), Hydrothermal Iron Oxide Copper-Gold and Related Deposits: A Global Perspective. PGC Publishing Adelaide Australia 1, pp. 9–25.

Heidarian, H., Alirezaei, S., Lentz, D.R., 2017. Chadormalu Kiruna-type magnetite apatite deposit, Bafq district, Iran: insights into hydrothermal alteration and petrogenesis from geochemical, fluid inclusion, and sulfur isotope data. Ore Geol. Rev. 83, 43–62. https://doi.org/10.1016/j.oregeorev.2016.11.031.

Hoefs, J., 2004. In: Stable Isotope Geochemistry, fifth ed. Springer Verlag, Berlin, p. 285p.

Hou, T., Charlier, B., Holtz, F., Veksler, I., Zhang, Z., Thomas, R., Namur, O., 2018. Immiscible hydrous Fe-Ca-P melt and the origin of iron oxide-apatite ore deposits. Nat. Commun. 9, 1–8. https://doi.org/10.1038/s41467-018-03761-4.

Huckriede, R., Kürsten, M., Venzlaff, H., 1962. Zur geologie des gebietes zwischen Kerman und Sagand (Iran). Beihefte zum Geologischen Jahrbuch 51, 197.

Jami, M., 2005. Geology, geochemistry and evolution of the Esfordi phosphate – iron deposit. Ph.D. Thesis. University of New South Wales, Bafq Area, Central Iran.

Jami, M., Dunlop, A.C., Cohen, D.R., 2007. Fluid inclusion and stable isotope study of Esfordi apatite-magnetite deposit, Central Iran. Econ. Geol. 102, 1111–1125. https://doi.org/10.2113/gsecongeo.104.1.140.

Kavoshgaran Consultant Engineers. 2009. Detailed exploration surveys and evaluation of Chahgaz iron ore deposit. 87 p.

Khoshnoodi, K., Behzadi, M., Gannadi-Maragheh, M., Yazdi, M., 2017. Alkali metasomatism and Th-REE-mineralization in the Choghart deposit, Bafq district, Central Iran. Geol. Croatica 70, 53–69. https://doi.org/10.4154/gc.2017.03.

Knipping, J., Webster, J.D., Simon, A.C., Holtz, F., 2019. Accumulation of magnetite by flotation on bubbles during decompression of silicate magma. Sci. Rep. 9, 3852. https://doi.org/10.1038/s41598-019-40376-1.

Knipping, J.L., Bilenker, L., Simon, A.C., Reich, M., Barra, F., Deditius, A., Lundstrom, C., Bindeman, I., Munizaga, R., 2015a. Giant Kiruna-type deposits form by efficient flotation of magmatic magnetite suspensions. Geol. 43, 591–594. https://doi.org/10.1130/G36650.1.

Knipping, J.L., Bilenker, L.D., Simon, A.C., Reich, M., Barra, F., Deditius, A.P., Wälle, M., Heinrich, C.A., Holtz, F., Munizaga, R., 2015b. Trace elements in magnetite from massive iron oxide-apatite deposits indicate a combined formation by igneous and magmatic-hydrothermal processes. Geochim. Cosmochim. Acta 171, 15–38. https://doi.org/10.1016/j.gca.2015.08.010.

Kyser, T.K., Lesher, C.E., Walker, D., 1998. The effects of liquid immiscibility and thermal diffusion on oxygen isotopes in silicate liquids. Contrib. Mineral. Petrol. 133 (4), 373–381. https://doi.org/10.1007/s004100050459.

La Cruz, N., Ovalle, J.T., Simon, A.C., Konecke, B.A., Barra, F., Leisen, M., Reich, M., Childress, T.M., 2020. The geochemistry of magnetite and apatite from the El Laco Kiruna-type iron oxide–apatite deposit, Chile: implications for ore genesis. Econ. Geol. 115 (7), 1461–1491. https://doi.org/10.5382/econgeo.4753.

Leake, B.E., Wooley, A.R., Arps, C.E.S., Birch, W.D., Gilbert, M.C., Grice, J.D., Hawthorne, F.C., Kato, A., Kisch, H.J., Krivovichev, V.G., Linthout, K., Laird, J., Mandarino, J.A., Maresch, W.V., Nickel, E.H., Rock, N.M.S., Schumacher, J.C., Smith, D.C., Stephenson, N.C.N., Ungaretti, L., Whittaker, E.J.W., Youzhi, G., 1997. Nomenclature of amphiboles: Report of the subcommittee on amphiboles of the International Mineralogical Association, Commission on new minerals and mineral names. Am. Mineral. 82, 1019–1037. https://doi.org/10.1180/minmag.1997.061.405.13.

Mehdipour, J., Harris, C., Rahgoshay, M., Moazzen, M., 2019. Combined igneous and hydrothermal source for the Kiruna-type Bafq magnetite-apatite deposits in Central Iran; trace element and oxygen isotope studies of magnetite. Ore Geol. Rev. 78, 590–604. https://doi.org/10.1016/j.oregeorev.2019.01.006.

Meinert, L.D., Dipple, G.M., Nicolescu, S., 2005. World skarn deposits: Econ. Geol. 100th Anniversary volume, 299-336. doi:10.5382/AV100.11.

Menard, J.J., 1995. Relationship between altered pyroxene diorite and the magnetite mineralization in the Chilean iron belt, with emphasis on the El Algarrobo iron deposits (Atacama region, Chile). Miner. Deposita 30 (3), 268–274. https://doi.org/10.1007/BF00196362.

Mohseni, S., Aftabi, A., 2015. Structural, textural, geochemical and isotopic signatures of synglaciogenic Neoproterozoic banded iron formations (BIFs) at Bafq mining district (BMD), Central Iran: the possible Ediacaran missing link of BIFs in Tethyan metallogeny. Ore Geol. Rev. 71, 215–236. https://doi.org/10.1016/j.oregeorev.2015.05.018.

Moore, F., Modabberi, S., 2003. Origin of Choghart iron oxide deposit, Bafq District, Central Iran: new isotopic and geochemical evidence. J. Sci. Islamic Republic Iran 14, 259–269.

Morimoto, N., Fabries, J., Ferguson, A.K., Ginzburg, I.V., Ross, M., Seifert, F.A., Zussman, J., 1989. Nomenclature of pyroxenes. Mineralogical 14, 198–221.

Mumin, A.H., Corriveau, L., Somarin, A.K., Ootes, L., 2007. Iron oxide copper-gold-type polymetallic mineralization in the Contact Lake Belt, Great Bear Magmatic Zone, Northwest Territories, Canada. Explor. Min. Geol. 16, 187–208. https://doi.org/10.2113/gsemg.16.3-4.187.

Nadoll, P., Angerer, T., Mauk, J.L., French, D., Walshe, J., 2014. The chemistry of hydrothermal magnetite: a review. Ore Geol. Rev. 61, 1–32. https://doi.org/10.1016/j.oregeorev.2013.12.013.

Nadoll, P., Mauk, J.L., Leveille, R.A., Koenig, A.E., 2015. Geochemistry of magnetite from porphyry Cu and skarn deposits in the southwestern United States. Miner. Deposita 50, 493–515. https://doi.org/10.1007/s00126-014-0539-y.

Naslund, H.R., Henriquez, F., Nyström, J.O., Vivallo, W., Dobbs, F.M., 2002. Magmatic iron ores and associated mineralisation: Examples from the Chilean High Andes and Coastal Cordillera. In: Porter, T.M., (Ed.), Hydrothermal Iron Oxide Copper-Gold and Related Deposits: A Global Perspective. PGC Publishing Adelaide Australia 2, pp. 207–226.

NIST, 2020. National Institutes of Science and Technology Report of Investigation Reference Material 8535a VSMOW2 Vienna Standard Mean Ocean Water 2. https://www-s.nist.gov/m-srmors/certificates/8535a.pdf.

Nyström, J.O., Billström, K., Henríquez, F., Fallick, A.E., Naslund, R.H., 2008. Oxygen isotope composition of magnetite in iron ores of the Kiruna type from Chile and Sweden. GFF 130 (4), 177–188. https://doi.org/10.1080/11035890801304177.

Nyström, J.O., Henríquez, F., 1994. Magmatic features of iron ores of the Kiruna-type in Chile and Sweden: ore textures and magnetite geochemistry. Econ. Geol. 89, 820–839.

Ovalle, J.T., La Cruz, N.L., Reich, M., Barra, F., Simon, A.C., Konecke, B.A., Morata, D., 2018. Formation of massive iron deposits linked to explosive volcanic eruptions. Sci. Rep. 8, 14855. https://doi.org/10.1038/s41598-018-33206-3.

Palma, G., Barra, F., Reich, M., Simon, A.C., Romero, R., 2020. Magnetite geochemistry of Andean iron oxide-apatite (IOA) deposits: a review. Ore Geol. Rev. 126, 103748 https://doi.org/10.1016/j.oregeorev.2020.103748.

Palma, G., Barra, F., Reich, M., Valencia, V., Simon, A.C., Vervoort, J., Romero, R., 2019. Halogens, trace element concentrations, and Sr-Nd isotopes in apatite from iron oxide-apatite (IOA) deposits in the Chilean iron belt: evidence for magmatic and hydrothermal stages of mineralization. Geochim. Cosmochim. Acta 246, 515–540. https://doi.org/10.1016/j.gca.2018.12.019.

Park Jr., C.F., 1961. A magnetite "flow" in northern Chile. Econ. Geol. 56 (2), 431–436. https://doi.org/10.2113/gsecongeo.56.2.431.

Pollard, P.J., 2006. An intrusion-related origin for Cu-Au mineralization in iron oxide-copper-gold (IOCG) provinces. Miner. Deposita 41, 179–187. https://doi.org/10.1007/s00126-006-0054-x.

Rajabi, A., 2012. Ore controlling parameters and genesis of sedimentary exhalative Zn-Pb (SEDEX type) deposits, Zarigan-Chahmir Area, East of Bafq, Central Iran. Ph.D. Thesis, Faculty of Science, Tarbiat Modarres University, Iran.

Rajabi, A., Canet, C., Rastad, E., Alfonso, P., 2015. Basin evolution and stratigraphic correlation of sedimentary-exhalative Zn-Pb deposits of the Early Cambrian Zarigan-Chahmir basin, Central Iran. Ore Geol. Rev. 64, 328–353. https://doi.org/10.1016/j.oregeorev.2014.07.013.

Ramezani, J., Tucker, R.D., 2003. The Saghand region, central Iran: U-Pb geochronology, petrogenesis and implications for Gondwana tectonics. Am. J. Sci. 303, 622–665. https://doi.org/10.2475/ajs.303.7.622.

Reed, M.H., 1997. Hydrothermal alteration and its relationship to ore fluid composition. In: Barnes, H.L. (Ed.), Geochemistry of Hydrothermal Ore Deposits, third ed. Wiley, New York, NY, pp. 303–365.

Reich, M., Simon, A.C., Deditius, A., Barra, F., Chryssoulis, S., Lagas, G., Roberts, M.P., 2016. Trace element signature of pyrite from the Los Colorados iron oxide-apatite (IOA) deposit, Chile: a missing link between Andean IOA and iron oxide copper-gold systems? Econ. Geol. 111 (3), 743–761. https://doi.org/10.2113/econgeo.111.3.743.

Rhodes, A.L., Oreskes, N., 1999. Oxygen isotope composition of magnetite deposits at El Laco, Chile: evidence of formation from isotopically heavy fluids. In Geology and ore deposits of the Central Andes. Soc. Econ. Geol. Spec. Publ. 7, 333–351.

Rhodes, A.L., Oreskes, N., Sheets, S., 1999. Geology and rare earth element geochemistry of magnetite deposits at El Laco, Chile. Soc. Econ. Geol. Spec Publ. 7, 299–332.

Rodriguez-Mustafa, M.A., Simon, A.C., Del Real, I., Thompson, J.F.H., Bilenker, L.D., Barra, F., Bindeman, I., 2020. A continuum from iron oxide-copper-gold (iocg) to iron oxide-apatite (ioa) deposits: evidence from Fe and O stable isotopes and trace element chemistry of magnetite. Econ. Geol. 115 (7), 1443–1459. https://doi.org/10.5382/econgeo.4752.

Rojas, P., Barra, F., Reich, M., Deditius, A., Simon, A., Uribe, F., Romero, R., Rojo, M., 2018a. A genetic link between magnetite mineralization and diorite intrusion at the El Romeral iron oxide-apatite deposit, northern Chile. Miner. Deposita 53, 947–966. https://doi.org/10.1007/s00126-017-0777-x.

Rojas, P., Barra, F., Deditius, A., Reich, M., Simon, A., Roberts, M., Rojo, M., 2018b. New contributions to the understanding of Kiruna-type iron oxide-apatite deposits revealed by magnetite ore and gangue mineral geochemistry at the El Romeral deposit, Chile. Ore Geol. Rev. 93, 413–435. https://doi.org/10.1016/j.oregeorev.2018.01.003.

Sadeghi Davati, V.A., 2008. Geochemical and genetic investigation of Choghart magnetite- apatite deposit. M.Sc thesis, University of Tehran, Iran. (In Persian).

Sadeghi, R., 2008. Geochemical and genetic investigation of North Anomaly iron ore (central Iran). M.Sc thesis, University of Tehran, Iran. (In Persian).

Salazar, E., Barra, F., Reich, M., Simon, A., Leisen, M., Palma, G., Rojo, M., 2020. Trace element geochemistry of magnetite from the Cerro Negro Norte iron oxide- apatite deposit, northern Chile. Miner. Deposita 55, 409–428. https://doi.org/10.1007/s00126-019-00879-3.

Saunders, A.D., Tarnery, J., 1991. Back-arc basins. In: Floyd, P.A. (Ed.), Oceanic Basalts. Blackie, Glasgow, pp. 219–263. doi:10.1007/978-1-4615-3540-9_10.

Schandl, E.S., Gorton, M.P., 2002. Application of high field strength elements to discriminate tectonic setting in VMS environments. Econ. Geol. 97, 629–642. https://doi.org/10.2113/gsecongeo.97.3.629.

Shamsipour, R., Khakzad, A., Rasa, I., Vosoughi-Abedini, M., 2008. Mineralogy and fluid inclusion studies of Chador-Malu iron ore deposit, Bafq. Central Iran. Res. J. Univ. Isfahan 29, 129–144 (In Persian).

Sillitoe, R.H., Burrows, D.R., 2002. New field evidence bearing on the origin of the El Laco magnetite deposit, northern Chile. Econ. Geol. 97, 1101–1109. https://doi.org/10.2113/gsecongeo.98.7.1497.

Simon, A.C., Kniping, J., Reich, M., Barra, F., Deditius, A.P., Bilenker, L., Childress, T., 2018. Kiruna-type iron oxide-apatite (IOA) and iron oxide copper-gold (IOCG) deposits form by a combination of igneous and magmatic-hydrothermal processes: evidence from the Chilean Iron Belt. SEG Spec. Publ. 21, 89–114. https://doi.org/10.5382/SP.21.06.

Simon, A.C., Pettke, T., Candela, P.A., Piccoli, P.M., Heinrich, C.A., 2004. Magnetite solubility and iron transport in magmatic-hydrothermal environments. Geochim. Cosmochim. Acta 68 (23), 4905–4914. https://doi.org/10.1016/j.gca.2004.05.033.

Stosch, H., Romer, R., Daliran, F., Rhede, D., 2011. Uranium-lead ages of apatite from iron oxide ores of the Bafq District, East-Central Iran. Miner. Deposita 46, 9–21. https://doi.org/10.1007/s00126-010-0309-4.

Stocklin, J., 1968. Structural history and tectonics of Iran: a review. AAPG Bull. 52, 1229–1258. https://doi.org/10.1306/5D25C4A5-16C1-11D7-8645000102C1865D.

Torab, F.M., Lehmann, B., 2007. Magnetite-apatite deposits of the Bafq district, Central Iran: apatite geochemistry and monazite geochronology. Mineral. Mag. 71, 347–363. https://doi.org/10.1180/minmag.2007.071.3.347.

Tornos, F., Velasco, F., Hanchar, J.M., 2016. Iron-rich melts, magmatic magnetite, and superheated hydrothermal systems: the El Laco deposit, Chile. Geol. 44 (6), 427–430. https://doi.org/10.1130/G37705.1.

Tornos, F., Velasco, F., Hanchar, J.M., 2017. The magmatic to magmatic-hydrothermal evolution of the El Laco deposit (Chile) and its implications for the genesis of magnetite-apatite deposits. Econ. Geol. 112 (7), 1595–1628. https://doi.org/10.5382/econgeo.2017.4523.

Travisany, V., Henriquez, F., Nyström, J.O., 1995. Magnetite lava flows in the Pleito-Melon District of the Chilean iron belt. Econ. Geol. 90, 438–444. https://doi.org/10.2113/gsecongeo.90.2.438.

Troll, V.R., Weis, F.A., Jonsson, E., Andersson, U.B., Majidi, S.A., Högdahl, K., Harris, C., Millet, M.A., Chinnasamy, S.S., Kooijman, E., Nilsson, K.P., 2019. Global Fe–O isotope correlation reveals magmatic origin of Kiruna-type apatite-iron-oxide ores. Nat. Commun. 10, 1–12. https://doi.org/10.1038/s41467-019-09244-4.

Velasco, F., Tornos, F., Hanchar, J.M., 2016. Immiscible iron-and silica-rich melts and magnetite geochemistry at the El Laco volcano (northern Chile): Evidence for a magmatic origin for the magnetite deposits. Ore Geol. Rev. 79, 346–366. https://doi.org/10.1016/j.oregeorev.2016.06.007.

Westhues, A., Hanchar, J.M., Whitehouse, M.J., Martinsson, O., 2016. New constraints on the timing of host-rock emplacement, hydrothermal alteration, and iron oxide-apatite mineralization in the Kiruna district, Norrbotten, Sweden. Econ. Geol. 111 (7), 1595–1618. https://doi.org/10.2113/econgeo.111.7.1595.

Westhues, A., Hanchar, J.M., LeMessurier, M.J., Whitehouse, M.J., 2017a. Evidence for hydrothermal alteration and source regions for the Kiruna iron oxide–apatite ore (northern Sweden) from zircon Hf and O isotopes. Geol. 45, 571–574. https://doi.org/10.1130/G38894.1.

Westhues, A., Hanchar, J.M., Voisey, C.R., Whitehouse, M.J., Rossman, G.R., Wirth, R., 2017b. Tracing the fluid evolution of the Kiruna iron oxide apatite deposits using zircon, monazite, and whole rock trace elements and isotopic studies. Chem. Geol. 466, 303–322. https://doi.org/10.1016/j.chemgeo.2017.06.020.

Williams, P.J., Barton, M.D., Johnson, D.N., Fontboté, L., De Haller, A., Mark, G., Oliver, N.H.S., Marschik, R., 2005. Iron oxide-copper-gold deposits: Geology, space-time distribution, and possible modes of origin. Econ. Geol. 100th Anniversary volume, 371–-405. doi:10.5382/AV100.13.

Whitney, D.L., Evans, D.W., 2010. Abbreviations for names of rock-forming minerals. Am. Mineral. 95, 185–187. https://doi.org/10.2138/am.2010.3371.

Winchester, J.A., Floyd, P.A., 1977. Geochemical discrimination of different magma series and their differentiation products using immobile elements. Chem. Geol. 20, 325–343. https://doi.org/10.1016/0009-2541(77)90057-2.